Extracellular matrix stiffness mediates insulin secretion in pancreatic islets via mechanosensitive Piezo1 channel regulated Ca^{2+} dynamics

Chelsea G. Johansen [a], Keifer Holcomb [a], Amit Sela [b], Stephanie Morrall [b], Daewon Park [c], Nikki L. Farnsworth [a,b,*]

[a] Department of Chemical & Biological Engineering, Colorado School of Mines, Golden, CO 80401, USA
[b] Quantitative Biosciences & Engineering, Colorado School of Mines, Golden, CO 80401, USA
[c] Department of Bioengineering, University of Colorado Denver Anschutz Medical Campus, Aurora, CO 80045, USA

ARTICLE INFO

ABSTRACT

The pancreatic islet is surrounded by ECM that provides both biochemical and mechanical cues to the islet β-cell to regulate cell survival and insulin secretion. Changes in ECM composition and mechanical properties drive β-cell dysfunction in many pancreatic diseases. While several studies have characterized changes in islet insulin secretion with changes in substrate stiffness, little is known about the mechanotransduction signaling driving altered islet function in response to mechanical cues. We hypothesized that increasing matrix stiffness will lead to insulin secretion dysfunction by opening the mechanosensitive ion channel Piezo1 and disrupting intracellular Ca^{2+} dynamics in mouse and human islets. To test our hypothesis, mouse and human cadaveric islets were encapsulated in a biomimetic reverse thermal gel (RTG) scaffold with tailorable stiffness that allows formation of islet focal adhesions with the scaffold and activation of Piezo1 in 3D. Our results indicate that increased scaffold stiffness causes insulin secretion dysfunction mediated by increases in Ca^{2+} influx and altered Ca^{2+} dynamics via opening of the mechanosensitive Piezo1 channel. Additionally, inhibition of Piezo1 rescued glucose-stimulated insulin secretion (GSIS) in islets in stiff scaffolds. Overall, our results emphasize the role mechanical properties of the islet microenvironment plays in regulating function. It also supports further investigation into the modulation of Piezo1 channel activity to restore islet function in diseases like type 2 diabetes (T2D) and pancreatic cancer where fibrosis of the *peri*-islet ECM leads to increased tissue stiffness and islet dysfunction.

Introduction

The pancreatic islets of Langerhans are clusters of hormone-producing cells that regulate blood glucose levels. Islet β-cells, which produce and secrete insulin to maintain blood glucose homeostasis, are the most abundant cell type [1]. The islet is surrounded by a unique extracellular matrix (ECM), composed primarily of networked type IV collagen and laminin [2]. Additionally, the long polysaccharide hyaluronan is found in abundance both around and within the islet [3,4]. The *peri*-islet ECM forms a dynamic microenvironment integrating mechanical and biochemical cues that promote islet survival and insulin secretion [2,5]. The pancreas is considered a soft tissue with a stiffness range of 0.1–1 kPa [5,6]. Changes in ECM stiffness play a role in the progression of several pancreatic diseases, such as pancreatic fibrosis seen in chronic pancreatitis and pancreatic ductal adenocarcinoma (PDAC), pancreatic inflammation where increased hyaluronan deposition leads to increased pancreatic ECM stiffness, and excessive ECM deposition in type 2 diabetes (T2D) where the pancreatic ECM stiffness increases to a range of 2–5 kPa and is associated with islet dysfunction [7–13]. In T2D, increased ECM deposition, specifically increases in type I and type III collagen, fibronectin, and hyaluronan lead to increases in tissue stiffness [10,14]. In PDAC, there is an imbalance between ECM

synthesis and degradation resulting in excess type I and type III collagen deposition, which increases tissue stiffness and supports cancer cell survival and proliferation [9,15–18]. The progression from a healthy pancreas to PDAC highlights increased stiffness due to fibrosis, implying altered mechanotransduction pathways [19]. Additionally, in early type 1 diabetes (T1D), significant accumulation of hyaluronan within and surrounding the islet has been observed, which may contribute to increased local tissue stiffness and the islet dysfunction commonly observed in preclinical T1D [3,4,20]. While numerous studies have emphasized the significance of the ECM architecture and biochemical composition in regulating islet function, less is known about the role of ECM mechanical properties in governing islet function [2,21–23].

Mechanotransduction signaling in β-cells operates through two main mechanisms: the interaction of integrins with specific ECM proteins in focal adhesions and the activation of mechanosensing cell surface ion channels, both of which initiate intracellular signaling cascades that regulate insulin secretion [24–26]. For example, previous research has shown increased stiffness of cell culture substrate causes dysfunction to insulin secretion, including a decrease in stimulation index (SI), in Min6-derived β-cell clusters via upregulation of the Rho-associated protein kinase (ROCK) integrin mediated mechanosensing pathway [6]. While activation of the ROCK signaling pathway upregulates the transcription factor β-catenin and regulates insulin gene expression, the link between mechanotransduction signaling and direct regulation of insulin secretion has not been explored [6]. Glucose stimulated insulin secretion (GSIS) in the β-cell is mediated by closure of the ATP-gated potassium channel (K_{ATP}) and depolarization of the β-cell membrane that stimulates an influx of Ca^{2+} [27,28]. Piezo1, a mechanosensitive stretch-activated non-selective cation channel, has recently been shown to be a key regulator of β-cell electrical activity, intracellular Ca^{2+}, and insulin secretion [26,29]. Additionally, previous research has revealed that opening of the Piezo1 channel triggered by changes in matrix stiffness, facilitates fibroblast adaptation and regulates oxidative stress-related processes in human intervertebral disc degeneration [30,31]. However, the role of Piezo1 in mediating stiffness induced dysfunction to GSIS has not been investigated.

The goal of this study is to determine the role of Piezo1 in mediating stiffness-induced changes in islet function and insulin secretion. We employed a biomimetic reverse thermal gel (RTG) encapsulation system to tightly control the stiffness of the islet microenvironment and enable the formation of islet focal adhesions with the scaffold to confer mechanical cues in 3D. We found that increased scaffold stiffness causes insulin secretion dysfunction mediated by increases in Ca^{2+} influx and altered Ca^{2+} dynamics via opening of the mechanosensitive Piezo1 channel. Additionally, inhibition of Piezo1 rescued GSIS in islets in stiff scaffolds. Understanding the specific signaling pathways underlying Piezo1 regulation of insulin secretion will expand our understanding of islet electrophysiology and how the pancreas microenvironment contributes to regulation of insulin secretion and will identify potential targets to restore islet function in pancreatic diseases where changes in ECM properties contribute to reduced islet function. Moreover, the results from this work will inform the design of islet transplantation scaffolds to improve graft function and treatment outcomes.

Materials and methods

RTG synthesis

Poly(serinol hexamethylene urea)–co-poly(N-isopropylacrylamide) (PSHU-PNIPAAm) was synthesized based on a previously described protocol [32,33]. Briefly, 6 mmol N-Boc serinol (Sigma-Aldrich, St. Louis, MO) and 6 mmol urea (Fisher Scientific, Hampton, NH) were dissolved in 6 mL of N-N-dimethylformamide (DMF) (Sigma-Aldrich, St. Louis, MO) in a 90 °C mineral oil bath with constant stirring. Under nitrogen atmosphere, hexamethylene diisocyanate (Sigma-Aldrich, St. Louis, MO) was added drop-wise to the reaction and allowed to react for

7 days protected from light. The reaction was precipitated thrice in anhydrous ethyl ether (Fisher Scientific, Hampton, NH) and dried via rotary evaporation on a Rotavapor R-100 (BUCHI, New Castle, DE). The solid was re-dissolved in DMF, precipitated twice in water, and lyophilized to yield poly(serinol hexamethylene urea) (PSHU).

PSHU (1 g) was dissolved in a 50:50 mixture of dichloromethane (Sigma-Aldrich, St. Louis, MO) and trifluoroacetic acid (30 mL total volume) (Sigma-Aldrich, St. Louis, MO) and was reacted with constant stirring at room temperature for 45 min. The acid was removed via rotary evaporation, the product was re-dissolved in DMF, and precipitated thrice in anhydrous ethyl ether. The product was redissolved in a small volume of 2,2,2-trifluoroethylene (Sigma-Aldrich, St. Louis, MO) after precipitation to yield de-protected PSHU (dPSHU).

Carboxylic acid-terminated PNIPAAm (PNIPAAm-COOH) was synthesized by reacting 5 g of poly(N-isopropylacrylamide) (Sigma-Aldrich, St. Louis, MO) and 0.06 g of 4,4-azobis(4-cyanovaleric acid) (Sigma-Aldrich, St. Louis, MO) in 10 mL DMF under nitrogen atmosphere for 3 h in a 68 °C with constant stirring. The product was precipitated four times in 60C water, dialyzed for 48 h in 3500 Da molecular weight cut-off (MWCO) dialysis tubing (21–152-9; Fisher Scientific, Hampton, NH), and lyophilized to yield a white product.

PNIPAAm was dissolved in 15 mL DMF and slowly added to a flask containing N-hydroxysuccinimide (Alfa Aesar, Ward Hill, MA) and N-ethyl-N'-(3-dimethylaminopropyl)carbodiimide hydrochloride (Sigma-Aldrich, St. Louis, MO) under a nitrogen atmosphere and was protected from light for 24 h at room temperature. dPSHU was dissolved in 1 mL DMF and added drop-wise to the conjugation reaction. After 24 h, the reaction was precipitated in 50 mL of anhydrous ethyl ether and dried via rotary evaporation. The final product was precipitated in room temperature dH_2O and dialyzed against dH_2O for 48 h in 12000 Da MWCO dialysis tubing (08–670-3A; Fisher Scientific, Hampton, NH). The product was lyophilized for 72 h to yield the reverse thermal gel (RTG) PSHU-PNIPAAm.

Nuclear magnetic resonance (NMR) spectroscopy

1H NMR spectra were collected on a 500 MHz liquid state NMR (JEOL USA, Inc., Peabody, MA). Spectra were collected in deuterated chloroform (DLM-7–100; Cambridge Isotope Laboratories, Inc., Andover, MA) and post-processed by means of Fourier Transform in iNMR (Nucleomatica).

Scanning electron microscopy (SEM)

RTG prepared at 2.5 wt%, 5 wt%, and 10 wt% in RPMI media were then snap frozen in liquid nitrogen and lyophilized for 24hr. Samples were imaged on carbon tape using a Phenom tabletop Scanning Electron Microscope (ThermoFisher Scientific, Waltham, MA). Analysis of the distance between RTG sheets, that was calculated by drawing straight lines between sheets in the images and measuring the distance, and the pore size, that was calculated as the average between two perpendicular diameters in the same pore, was done in ImageJ (NIH). Three gel samples were quantified for each RTG wt% (n = 3).

Rheology

200 μL of RTG prepared at 2.5 wt%, 5 wt%, and 10 wt% in RPMI media were placed between a 20.0 mm 2.0° cone and Peltier plate on a Discovery Hybrid Rheometer (HR-3, TA Instruments, New Castle, DE). Samples were run through a temperature sweep from 25 °C to 40 °C using a step size of 5 °C under an oscillatory strain of 0.5 %, angular frequency of 10 rad/s, and frequency of 1.6 Hz. We determined the temperature sensitive phase transition and stiffness of the RTG from the storage modulus readings (n = 6).

RTG diffusivity via fluorescence recovery after photobleaching (FRAP)

RTG prepared at 2.5 wt%, 5 wt%, 10 wt% and 15 wt% in RPMI media were gelled in 7 mm glass-bottom dishes at 37 °C for 10 min. RTG gels were then submerged and incubated in either 1.25 μM Lucifer Yellow CH dipotassium salt (Sigma-Aldrich, St. Louis, MO), 12.5 μM rhodamine 123 (Fisher Scientific, Hampton, NH), or 5 μM 10kMW dextran, Alexa Fluor 647 (Fisher Scientific, Hampton, NH) for 24hr at 37 °C. FRAP was performed on a Leica STELLARIS 5 LIAchroic laser supply unit with a 40X water immersion objective (numerical aperture = 1.1). On the microscope, a region of interest (ROI) was defined in the middle of the RTG sample with a diameter of 15 μm, ten pre-bleach ROI images were taken, then the ROI was bleached. Lucifer yellow, rhodamine 123, and dextran were excited using a 488 nm, 514 nm, or 638 nm solid state laser, respectively, and emission was collected using HyD spectral detectors. Post-bleach images were acquired for 4 min for each sample. Diffusivity was calculated using the previously described equation below [34].

$$D_{confocal} = \frac{r_e^2 + r_n^2}{8\tau_{1/2}} \qquad (1)$$

where D is the confocal diffusion coefficient, r_e is the nominal ROI radius, r_n is the effective radius or the spreading radius of post-bleach profile, and $\tau_{1/2}$ is the half time of recovery. For all samples, three separate areas were averaged for a single n value (n = 5).

Animal care

All experiments using mice were performed at the University of Colorado Anschutz Medical Campus and in compliance with the guidelines and relevant laws set by the University of Colorado and the National Institutes of Health guide for the care and use of Laboratory animals. All performed procedures were approved by the University of Colorado Institutional Animal Care and Use Committee (Protocol 00929). Mice were housed in a temperature- and light-controlled environment with 12-hour light–dark cycles, and they were provided access to food and drink ad libitum. C57Bl/6 or NOD mice were purchased from the Jackson Laboratories (strain #000664) at 8 weeks of age.

Islet isolation and culture

For all experiments, islets were isolated from 8 to 16-week-old female C57BL/6 mice. Animals were injected with 100 mg/kg ketamine and 8 mg/kg xylazine and euthanized via exsanguination. Islets were isolated by injecting the pancreas with 12.5 mg/mL collagenase, pancreas removal, and enzymatic digestion at 37C. Islets were hand-picked into 1640 RPMI Medium with 1X with L-glutamine and 25 mM HEPES (Fisher Scientific, Hampton, NH) with 10 % fetal bovine serum (Fisher Scientific, Hampton, NH), 10,000 U/mL Penicillin and 10,000 μg/mL Streptomycin (Sigma-Aldrich, St. Louis, MO) and incubated at 37 °C and 5 % CO$_2$ for a minimum of 3 h before commencing experiments. Islets that were clear of any excess pancreatic tissue and were consistent in color and shape based on inspection through a microscope were selected for use in experiments.

Human islets

Human islets were obtained from the Integrated Islet Distribution Program (IIDP) from the following donors as outlined in Table 1:

Human donor tissue is de-identified through the IIDP and is therefore exempt from requiring human subjects research protocols. Islets that were clear of any excess pancreatic tissue and were consistent in color and shape based on inspection through a microscope were selected for use in experiments.

Islet viability

C57BL/6 mouse islets were encapsulated in RTG or freely cultured (unencapsulated) in RPMI media for 24 h at 37 °C under humidified 5 % CO$_2$. Each encapsulated RTG sample contained 10 islets in 50uL RTG with 2 mL RPMI media and each unencapsulated sample contained 10 islets in 2 mL RPMI media. Prior to imaging, samples were incubated with BMHH imaging buffer containing 125 mM NaCl, 5.7 mM KCl, 2.5 mM CaCl$_2$, 1.2 mM MgCl$_2$, 10 mM HEPES in dH$_2$O, pH 7.4, with 0.1 % bovine serum albumin with 15uL/mL propidium iodide and 15uL/mL fluorescein diacetate for 10 min. Imaging was performed on a Leica STELLARIS 5 Confocal Microscope with LIAchroic laser supply unit, and a 40X water immersion objective. 488 nm and 514 nm solid state lasers were used for excitation and emission was collected with HyD spectral detectors. All islets were imaged as a z-stack consisting of four images 10 μm apart and live/dead cells were counted manually in ImageJ (NIH) for 10 islets per mouse (n = 5).

Insulin secretion enzyme-linked immunosorbent assay (ELISA)

C57BL/6 mouse islets were encapsulated in RTG or unencapsulated and cultured for 24 h as previously described. Each encapsulated RTG sample contained 5 islets in 200uL RTG with 2 mL RPMI media and each unencapsulated sample contained 5 islets in 2 mL RPMI media. Each treatment was run in triplicate for a single experiment. Samples were then incubated with Krebs-Ringer buffer containing 88.8 mM NaCl, 5 mM NaHCO$_3$, 5.8 mM KCl, 1.2 mM KH$_2$PO$_4$, 2.5 mM CaCl$_2$, 1.2 mM MgSO$_4$, 10 mM HEPES in dH$_2$O, pH 7.4, with 0.1 % bovine serum albumin with 2 mM glucose for 1 h, the 2 mM solution was aspirated and replaced with fresh 2 mM glucose, 20 mM glucose, or 20 mM glucose with 20 mM KCl for an additional hour. In some experiments, mechanosensitive and stretch-activated ion channel inhibitor GsMTx-4 (ab141871; Abcam, Waltham, MA) was added to the glucose solution at a concentration of 2.5 μM. Supernatant was collected for analysis of secreted insulin. Islets were collected by placing the RTG on ice to reverse gelation, islets were hand picked out of the RTG solution and lysed by freezing in 2 % Triton X-100 in dH$_2$O. RTG solution was also collected to measure residual insulin secreted into the RTG that did not diffuse into the bulk media. Insulin was measured with a mouse ultra-sensitive insulin ELISA kit (80-INSMS-E10; ALPCO, Salem, NH) per the manufacturer's instructions. Each treatment was run in triplicate for a single experiment and run in triplicate in the ELISA. Data is reported as secretion (supernatant) normalized to content (lysate) for each sample. Stimulation index (SI) was calculated as the ratio of insulin secretion at 2 mM to 20 mM glucose (n = 5).

Table 1

Human cadaveric islet donor demographics and isolated islet viability and purity for islets obtains through the Integrated Islet Distribution Program (IIDP).

RRID#	Viability	Purity	Stimulation index (2 mM:20 mM)	Age	Sex	Ethnicity/Race
SAMN34075901	90.5 %	83 %	3.2148	39	Male	White
SAMN34130383	100 %	95 %	5.9528	42	Female	Hispanic/Latino
SAMN34411471	94 %	92 %	2.0476	45	Male	White
SAMN36705973	96 %	95 %	2.6048	36	Female	Black/African American
SAMN36823227	93 %	77 %	1.8522	41	Female	White

Phosphofructokinase (PFK) assay

C57BL/6 mouse islets were encapsulated in RTG or unencapsulated and cultured for 24 h as previously described. Each encapsulated RTG sample contained 100 islets in 200uL RTG with 4 mL RPMI media and each unencapsulated sample contained 100 islets in 4 mL RPMI media. Samples were then incubated with Krebs-Ringer buffer with 2 mM glucose for 1 h, the 2 mM solution was aspirated and replaced with fresh 11 mM glucose for an additional hour. Islets were collected from the RTG and lysed in lysis buffer containing 100 mM NaCl, 50 mM Tris-HCl, 10 mM $MgCl_2$, and 1X protease and phosphatase inhibitors (Thermo-Fisher Scientific, Waltham, MA). The lysate samples were sonicated for 1 min and were freeze thawed once in liquid nitrogen. The Phospho-fructokinase (PFK) Activity Colorimetric Assay Kit (MAK093-1KT; Sigma-Aldrich, St. Louis, MO) was used according to manufacturer's instructions. All samples were analyzed in triplicate. Data is reported as milliunits of PFK activity per mL of sample (n = 5).

Western blotting

C57BL/6 mouse islets were encapsulated in RTG or unencapsulated and cultured for 24 h as previously described. Each encapsulated RTG sample contained 100 islets in 200uL RTG with 4 mL media and each unencapsulated sample contained 100 islets in 4 mL RPMI media. Samples were then incubated with Krebs-Ringer buffer with 2 mM glucose for 1 h, the 2 mM solution was aspirated and replaced with fresh 11 mM glucose for an additional hour. Min6 cells were treated with 5 μM pyrintegrin (HY-13306; MedChemExpress, Monmouth Junction, NJ) in 11 mM glucose for 1hr as a positive control for β-cell integrin interactions. For the Piezo1 western blot analysis, C57BL/6 mouse islets were encapsulated in RTG or unencapsulated and cultured for 24 h as previously described. Each encapsulated RTG sample contained 100 islets in 200uL RTG with 4 mL RPMI media and each unencapsulated sample contained 100 islets in 4 mL RPMI media. Samples were then incubated with Krebs-Ringer buffer with 2 mM glucose for 1 h, the 2 mM solution was aspirated and replaced with fresh 2 mM glucose or 20 mM glucose for an additional hour. Islets and Min6 cells were collected and lysed in lysis buffer containing 1X protease and phosphatase inhibitors (ThermoFisher Scientific, Waltham, MA). Protein content was measured using the Pierce BCA Protein Assay Kit (PI23225; Fisher Scientific, Hampton, NH) according to the manufacturer's instructions. All samples were normalized to protein content using the results from a BCA assay and Ponceau S solution (P7170; Sigma-Aldrich, St. Louis, MO) staining. Samples were run on 4–15 % mini-PROTEAN® TGX protein gels (Bio-Rad, Hercules, CA) and transferred to a PVDF (Azure Biosystems, Dublin, CA) membrane. PVDF membranes were blocked in chemi-blot blocking buffer (Azure Biosystems, Dublin, CA) for 2hr and probed with either anti-RhoA (sc-418; Santa Cruz Biotechnology, Santa Cruz, CA) at a dilution of 1:200 or anti-Piezo1 (15939–1-AP; Proteintech, Rosemont, IL) at a dilution of 1:500 for > 2hr at 4 °C. Blots were washed in washing buffer (1X PBS with 0.1 % Tween) 3x prior to the addition of either secondary anti-mouse (626520; Fisher Scientific, Hampton, NH) horseradish peroxidase-conjugated antibodies diluted to 1:1000 or secondary anti-rabbit (102649–670; VWR, Radnor, PA) horseradish peroxidase-conjugated antibodies diluted to 1:10,000 for 2hr at room temperature. The membranes were washed in washing buffer 3x and incubated with Radiance Plus (Azure Biosystems, Dublin, CA) for 2 min in the dark. All membranes were imaged using an Azure c600 imaging system (Azure Biosystems, Dublin, CA) and protein quantification was performed in ImageJ using densitometric analysis (n = 4).

For the active Rho western blot analysis, C57BL/6 mouse islets were encapsulated in RTG or unencapsulated and cultured for 24 h as previously described. Each encapsulated RTG sample contained 100 islets in 200uL RTG with 4 mL RPMI media and each unencapsulated sample contained 100 islets in 4 mL RPMI media. Samples were then incubated with Krebs-Ringer buffer with 2 mM glucose for 1 h, the 2 mM solution was aspirated and replaced with fresh 11 mM glucose for an additional hour. Samples were lysed and total protein content in each sample was normalized by dilution after quantification with a BCA assay. An Active Rho Pull-Down and Detection kit (16116; ThermoFisher Scientific, Waltham, MA) was then used according to manufacturer's instructions. The positive and negative control samples from the Active Rho Pull-Down Kit were unencapsulated islets treated with either GTPδS or GDP to activate or inactivate Rho in the samples, respectively. All membranes were imaged using an Azure c600 imaging system (Azure Biosystems, Dublin, CA) and protein quantification was performed in ImageJ using densitometric analysis (n = 4).

Ki-67 immunofluorescence

Mouse islets were treated as previously described for 24 h. Each encapsulated RTG sample contained 10 islets in 50uL RTG with 2 mL RPMI media and each unencapsulated sample contained 10 islets in 2 mL RPMI media. Islets encapsulated in RTG or freely cultured islets were directly fixed in 4 % paraformaldehyde for 10 min then blocked for 5 min at 37 °C in PBS with 5 % normal donkey serum (NDS) and 0.25 % Triton-X-100. Antigen retrieval was performed using 1x citrate buffer. All samples were incubated at 60 °C overnight with gentle shaking. Samples were blocked again for 5 min. To study Ki-67 proliferation, samples were incubated for 2 h at 37 °C with a mouse anti-Ki-67 primary antibody (550609; BD Biosciences, San Jose, CA) and a rabbit monoclonal to insulin primary antibody (ab181547; Abcam, Waltham, MA) diluted 1:10 and 1:1000, respectively, in PBS with 5 % NDS and 0.25 % Triton-X-100. Samples were then incubated for 2 h at 37 °C with an Alexa Fluor 488 donkey anti-mouse secondary antibody (R37114; Fisher Scientific, Hampton, NH) and an Alexa Fluor 568 goat anti-rabbit secondary antibody (A11011; Fisher Scientific, Hampton, NH) diluted 1:1000 and 1:100, respectively, in PBS with 5 % NDS and 0.25 % Triton-X-100. Samples were imaged on a Leica STELLARIS 5 Confocal Microscope with LIAchroic laser supply unit with a 40X water immersion objective using 405 nm, 488 nm, 514 nm, and 561 nm solid state lasers and HyD spectral detectors. All islets were imaged as a z-stack consisting of four images 10 μm apart. Cells that were both insulin-positive and had visible Ki-67-stained nuclei were counted manually in ImageJ (NIH) (n = 4).

Reactive oxygen species (ROS)

The was a generous gift from Dr. Amelia Linnemann, where levels of ROS in the cell are determined by the ratio of unoxidized excitation/emission at 488 nm and 509 nm to the oxidized excitation/emission at 405 nm and 509 nm as previously described [35]. Isolated islets were washed with PBS followed by distention with Accutase (A1110501; Fisher Scientific, Hampton, NH) at 37 °C for 30 s. Accutase was inactivated with islet media, islets were washed with PBS and adenovirus was added to islet media at 2×10^7 viral particles per 100 islets for at least 18hr. Islets were then encapsulated in RTG or unencapsulated and cultured for 24 h as previously described. Each encapsulated RTG sample contained 10 islets in 50uL RTG with 2 mL RPMI media and each unencapsulated sample contained 10 islets in 2 mL RPMI media. Islets were then treated with 2 mM glucose solution for 10 min prior to the start of imaging, then the 2 mM glucose solution was replaced with fresh 20 mM glucose solution for 10 min and islets were imaged again at the higher glucose concentration. Data represents the average ROS stimulation, calculated as the ratio of ROS production at 2 mM to 20 mM glucose for each individual islet (n = 4).

Intracellular Ca^{2+} imaging and analysis

Ins-CreER GCaMP mice, which express the GCaMP calcium sensor specifically in β-cells, were a generous gift from Dr. Richard Benninger where changes in fluorescence intensity demonstrate changes in

intracellular Ca^{2+} flux post tamoxifen induction [36]. Isolated islets were encapsulated in RTG or unencapsulated and cultured for 24 h as previously described. Each encapsulated RTG sample contained 10 islets in 50uL RTG with 2 mL RPMI and each unencapsulated sample contained 10 islets in 2 mL RPMI media. The next day, islets were incubated in BMHH buffer containing 2 mM glucose at 37 °C for 1hr in the dark. All samples were imaged on a Leica STELLARIS 5 Confocal Microscope with LIAchroic laser supply unit with a 40X water immersion objective using a 488 nm solid state lasers and HyD spectral detectors. Islets were imaged at 37 °C, where images were acquired every second for 50 min for unencapsulated islets and for 1hr for encapsulated islets. Image acquisition began in 2 mM glucose for approximately 5 min, then 11 mM glucose was added for 25 min, then 20 mM glucose was added for 25 min, and finally 10 mM KCl was added for 5 min.

For each cell in an islet, the fluorescence intensity was extracted by taking a hand drawn region of interest around all observable GCaMP expressing cells and obtaining the intensity values over time. The background fluorescence signal was subtracted from the raw fluorescence intensity data for each cell. The background corrected fluorescence intensity for each cell was then normalized against its average intensity in the first 40 s of captured data, taken at 2 mM glucose, before any stimulation was applied. Normalization was performed to control for the natural variation in the quantity of Ca^{2+} indicator present in each β-cell. Normalized Ca^{2+} data for five cells from a single islet was selected as representative data for each condition (Fig. 6A-I).

The fraction of islet area active at 2 mM glucose was calculated in ImageJ (NIH) for 4–8 islets per condition over n = 3 independent experiments. Cells that qualified as 'active' had a $\geq$ 30 % increase in fluorescence intensity over a single Ca^{2+} peak at 2 mM glucose stimulation when compared to the same cell at its zero timepoint. The fraction of active islet area was then calculated as the ratio of the sum of the area of active cells at 2 mM glucose divided by the total islet area.

To calculate the area under the first phase curve (AUC) for the transition from 2 mM to 11 mM glucose, we first identified the end of the 1st phase response following an 11 mM glucose stimulus. Briefly, using a custom Python script openly available on Github [37], the normalized data was smoothed to reduce local oscillations. The SciPy library was then used to find all local minima and highly prominent maxima, and the script identified the first prominent maxima following the stimulus as the 1st phase. The program then selected the subsequent local minimum as the most likely potential endpoint for the 1st phase stimulus response. AUC was calculated for every cell with identifiable Ca^{2+} signal for each condition tested as described above.

When then determined the amplitude and frequency of second phase Ca^{2+} oscillations after stimulation with 11 mM glucose. We identified the local minimum and maximum of the smoothed data by determining all points in which the derivative changed from positive to negative. Oscillation period was then calculated as the median number of minutes passed between each maximum for a given cell. We compared the period in all of our conditions to that of the literature to ensure that the selected smoothing parameters are successfully identifying the second phase oscillations in all treatment groups [38]. Frequency was calculated from our determined oscillation period and compared between groups as previously described. Oscillation amplitude calculations were made using the difference in arbitrary units at each identified maximum and its neighboring minima. This average difference in arbitrary units between the maximum and its two neighboring minima, or the single difference when only one minimum was present, was then divided by two to establish the amplitude of the sinusoidal oscillations.

Statistical analysis

Data represent the average over all mice for each measurement with error bars representing standard error unless otherwise noted. Statistics were performed using Origin software (OriginLabs, Northampton, MA). Two sample *t*-test, one-way and two-way ANOVA with Tukey's post hoc analysis were performed as indicated. A p-value of < 0.05 or 95 % confidence intervals were considered statistically significant.

Results

RTG synthesis and characterization

^{1}H NMR was used to confirm the conjugation of PNIPAAm to PSHU. The presence of methyl and methylene protons at 1.10 and 1.60 ppm, respectively, signify proper conjugation of the PNIPAAm onto the PSHU backbone (Fig. 1A). Our NMR results were verified with previously published NMR spectra for PSHU-PNIPAAm [39,40]. The structural characterization of the RTG was conducted via SEM imaging (Fig. 1B). Cross-sectional images of 2.5 wt%, 5 wt%, and 10 wt% RTGs revealed interconnected highly porous sheets. The pore size and relative distance between sheets was measured for each RTG formulation. The pore size decreased with increasing RTG wt%, where the pore size of 10 wt% RTG was statistically lower than 2.5 wt% RTG (p = 0.014, Fig. 1C). Further, the average distance between sheets increased from 2.5 wt% to 5 wt% and 10 wt% RTG (p = 0.002, p = 0.05, Fig. 1D).

The temperature-dependent phase transition of the RTG was determined rheologically by measuring the storage modulus under temperature sweep from 20 to 40 °C. Between 30 and 35 °C, a 17.5 % $\pm$ 1.5 % increase in storage modulus was noticed, indicating the transition from a solution at room temperature to a polymeric gel as the temperature rises (Fig. 2A). Also, we note the slight increase in opacity from 25 to 37 °C as a secondary indicator of the phase transition (Fig. 2B) as previously recorded in literature [32,41]. To determine our ability to tune scaffold stiffness, equilibrium storage modulus at 40 °C (Fig. 2C) was calculated from the rheology data in Fig. 2A for RTG samples with incrementally increased wt% RTG. The equilibrium storage modulus significantly increased with increasing RTG wt% (p < 0.0001 for 2.5-15 wt%, p = 0.022 for 2.5-10 wt%, Fig. 2C). Of note, the 10 wt% RTG (1.17 kPa) was more than 2x stiffer than the 5 wt% RTG (0.475 kPa).

To determine if increasing wt% impacts diffusivity within the RTG, diffusivities of rhodamine 123 (cationic dye), lucifer yellow (anionic dye), and a fluorescently labeled dextran through various RTG wt%s were determined via FRAP at 37 °C (Fig. 2D). There was no significant difference between the diffusion coefficients of either dye through the 5 wt% and 10 wt% RTG samples (Fig. 2E-G). The 2.5 wt% RTG sample diffusivity was significantly higher than the 5 wt%, 10 wt%, and 15 wt% RTG samples for all dye solutions (p < 0.0001 for lucifer yellow and rhodamine 123, Fig. 2E-F, p < 0.015 for dextran, Fig. 2G). Overall, the RTG characterization data confirms that the RTG scaffold gels at body temperature and can be tuned to specific stiffness without impacting diffusivity in higher stiffness RTG formulations.

RTG scaffolds support islet function and transduce mechanical cues to the islet

To determine the suitability of the RTG scaffold for islet culture and investigation of mechanotransduction signaling, we characterized islet survival, stress, and formation of focal adhesions with the 3D RTG scaffold. There was no significant difference in islet viability with any RTG wt% tested at 24 or 48 h compared to unencapsulated islets (Fig. 3A-B). This supports that RTG encapsulation maintains islet viability similar to the NoRTG control. To determine if increased RTG stiffness leads to islet dysfunction due to ER stress or membrane rupture, we next measured ROS levels using a viral ROS sensor, roGFP2, as a readout of damage-associated molecular patterns (DAMPS), which are released upon membrane rupture and islet stress and correlate with ROS levels in the cell (Fig. 3C) [42,43]. There was no statistically significant ROS production in any of the treatment groups when compared to the NoRTG control (Fig. 3D). The positive control, hydrogen peroxide treatment, was significantly higher than the NoRTG (p = 0.002), 5 wt% (p = 0.002) and 10 wt% (p < 0.0005) conditions, verifying the
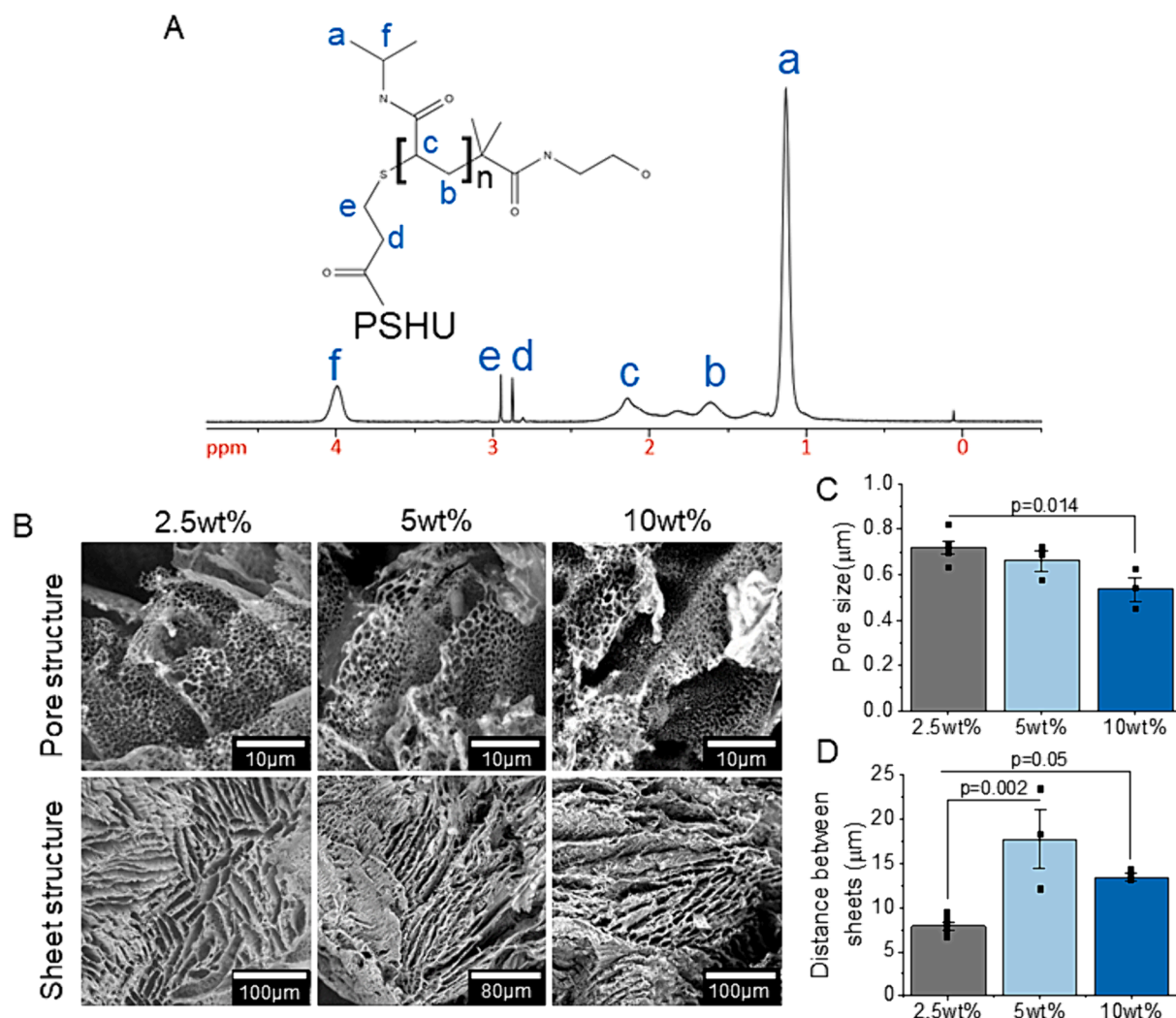
Fig. 1. Chemical structure and morphological analysis of varied wt% RTG with corresponding characterization. (A) Conjugation of PNIPAAm onto the PSHU backbone was verified via the (a) methyl and (b) ethyl proton spectra at 1.10 and 1.60 ppm, respectively. Further analysis of the other (c) ethyl proton spectra confirmed the structure of PNIPAAm and the presence of the (d,e) ethyl and (f) propyl proton spectra were also matched to literature. (B) SEM images of the pore and sheet structure of 2.5 wt%, 5 wt%, and 10 wt% RTG samples (n = 3). (C) Mean pore size, and (D) the distance between sheets expressed in microns, for the 2.5 wt%, 5 wt%, and 10 wt% RTG as measured from the SEM images represented in B. Error bars represent the mean +/- SEM. p < 0.05 indicates statistical significance as determine by ANOVA with Tukey's post hoc analysis.

functionality of the ROS sensor in transfected islets. Rho-GTPases, like RhoA, mediate transduction of external forces like stiffness to internal changes in cellular function [44]. When integrins bind to ECM proteins in focal adhesions, they undergo conformational changes that lead to the activation of intracellular signaling cascades via phosphorylation, like Rho activation [45]. Rho is considered active when bound to GTP and inactive when bound to GDP. To ensure our RTG scaffold supports integrin interactions and the formation of focal adhesions with the islet, we measured active Rho expression and total RhoA expression as evidence of activated integrin interactions in our samples (Fig. 3E-F, Supplemental Figure S2A-D). The amount of active Rho expression, and thus active integrin interactions, in whole mouse islets encapsulated in 5 wt% and 10 wt% RTG was significantly higher than the GDP treated, inactive Rho negative control (p = 0.043, p = 0.030, Fig. 3E-F). The amount of RhoA expression in mouse islets encapsulated in 10 wt% RTG was significantly higher than unencapsulated NoRTG islets (p = 0.005, Supplemental Figure S2A-B). In human islets, the amount of RhoA expression increases with increasing RTG stiffness when normalized to the NoRTG condition (Supplemental Figure S2C-D). To confirm the proper use of the RhoA antibody and expression of RhoA in our samples, we used Min6 cells cultured with pyrintegrin, a β1 integrin agonist, and

untreated Min6 cells. There is an increase in RhoA expression and integrin interaction in the pyrintegrin treated Min6 cells versus the untreated Min6 cells (Supplemental Figure S2E-F). Overall, our data confirms activation of integrins by the RTG in both mouse and human islets encapsulated in RTG.

Dysfunction to insulin secretion in mouse and human islets with increasing RTG stiffness

To determine changes in insulin secretion with changes in RTG stiffness, isolated mouse islets were encapsulated in RTG with increasing wt% and stiffness. We then assessed whether increases in RTG stiffness affect mouse and human islet function as measured by GSIS. The presented GSIS data is a measure of insulin secreted to the bulk media and insulin inside the RTG scaffold. In unencapsulated mouse islets (NoRTG), increased insulin secretion occurs at high 20 mM glucose compared to basal 2 mM glucose (p = 0.021, Fig. 4A). Encapsulation in 2.5 wt% RTG increased insulin secretion at both basal (2 mM) and high glucose (20 mM) conditions compared to unencapsulated NoRTG controls (p = 0.012, Fig. 4A). As RTG wt% and scaffold stiffness increases from 2.5 to 5 wt%, basal insulin secretion was similar to the NoRTG
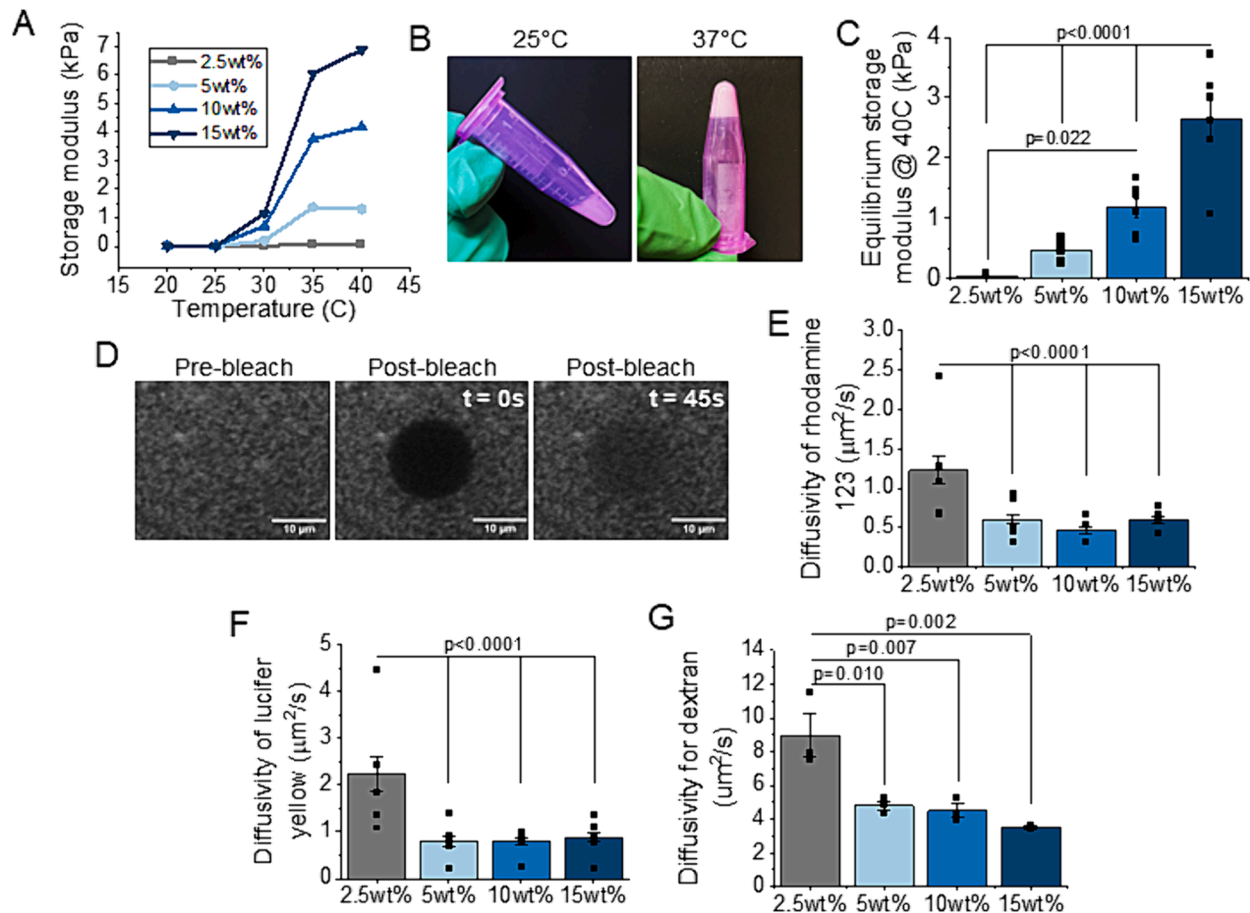
Fig. 2. Mechanical characterization of varied wt%'s of RTG. (A) Temperature dependent phase transition of 2.5 wt%, 5 wt%, 10 wt% and 15 wt% RTG represented by the increase in storage modulus from 20 to 40 °C as measured by rheology (n = 5). (B) Representative images of a tilt test depicting the 10 wt% RTG phase transition from 25 °C to 37 °C. (C) Equilibrium storage modulus data of 2.5 wt%, 5 wt%, 10 wt% and 15 wt% RTG at 40 °C as measured by rheology (n = 5). (D) Representative images of pre- and post-photobleaching at t = 0 s and t = 45 s in a 10 wt% RTG sample incubated with rhodamine 123. Calculated diffusivity of (E) rhodamine 123, (F) lucifer yellow, and (G) fluorescently labeled dextran through 2.5 wt%, 5 wt%, 10 wt% and 15 wt% RTG samples as determine via FRAP experiments represented in D (n = 3–5). Error bars represent the mean +/- SEM. p < 0.05 indicates statistical significance as determine by ANOVA with Tukey's post hoc analysis. (For interpretation of the references to color in this figure legend, the reader is referred to the web version of this article.)

condition; however, 20 mM insulin secretion was decreased compared to the 2.5 wt% conditions (p = 0.042, Fig. 4A). As RTG wt% increased further to 10 wt% RTG, there is an increase in insulin secretion at basal, 2 mM glucose compared to unencapsulated NoRTG controls, while insulin secretion at 20 mM glucose did not further decrease compared to 5 wt% RTG. The stimulation index (SI) decreased with increasing scaffold stiffness, where the 10 wt% RTG condition was significantly lower than the NoRTG control (p = 0.029, Fig. 4B), further demonstrating dysfunction to insulin secretion with increasing stiffness. Similarly, in human islets encapsulated in 10 wt% RTG, there is a decrease in insulin secretion at 20 mM glucose compared to the 2.5 wt% RTG (Fig. 4C). Overall, our data supports dysfunction to insulin secretion with a decrease in insulin secretion at 20 mM glucose with increasing scaffold stiffness.

Previous studies in endothelial cells and hepatocellular carcinoma cells have shown that increased matrix stiffness enhances cell proliferation [46,47]. To determine if islet proliferation contributed to the observed changes in insulin secretion with increased matrix stiffness, we stained for the proliferation marker Ki-67 in both mouse and human islets. There was no evident Ki-67 staining in the nuclei of the insulin-positive β-cells (Supplemental Figure S1A-B). HEK-293 cell samples showed Ki-67 staining as a positive control (Supplemental Figure S1C).

RTG stiffness induced changes in Ca²⁺ dynamics and insulin secretion regulated by Piezo1

To understand how mechanical cues are transduced to the islet from the RTG and determine if Piezo1 plays a role in mechanotransduction signaling, whole islet Piezo1 protein expression was analyzed via western blot (Fig. 5A-B). We confirmed expression of Piezo1 in isolated islets and showed no statistically significant differences in Piezo1 expression across any test conditions (Fig. 5A-B). This supports the presence of the Piezo1 channel in islets encapsulated in RTG that could transduce mechanical cues from the RTG surrounding the islet to induce changes in insulin secretion.

To determine the role of Piezo1 in mediating mechanotransduction regulation of insulin secretion we utilized the Piezo1 peptide inhibitor GsMTx-4, which holds Piezo1 channels closed under mechanical stress, preventing stiffness induced membrane depolarization and Ca²⁺ influx [48,49]. In the NoRTG control, GsMTx-4 (inhibition of Piezo1) did not significantly impact insulin secretion. At 2 mM glucose in the 10 wt% RTG, there was a decrease in insulin secretion with GsMTx-4 inhibition compared to the control (no inhibitor) (p < 0.001, Fig. 5C). At 20 mM glucose, there is no significant difference between GSIS without or with GsMTx-4 in the NoRTG control, 2.5 wt% RTG, or the 10 wt% RTG. Addition of GsMTx-4 in 10 wt% RTG samples rescued the SI to similar levels as in the NoRTG control (Fig. 5D), further supporting a role for Piezo1 in regulating stiffness induced dysfunction to insulin secretion.
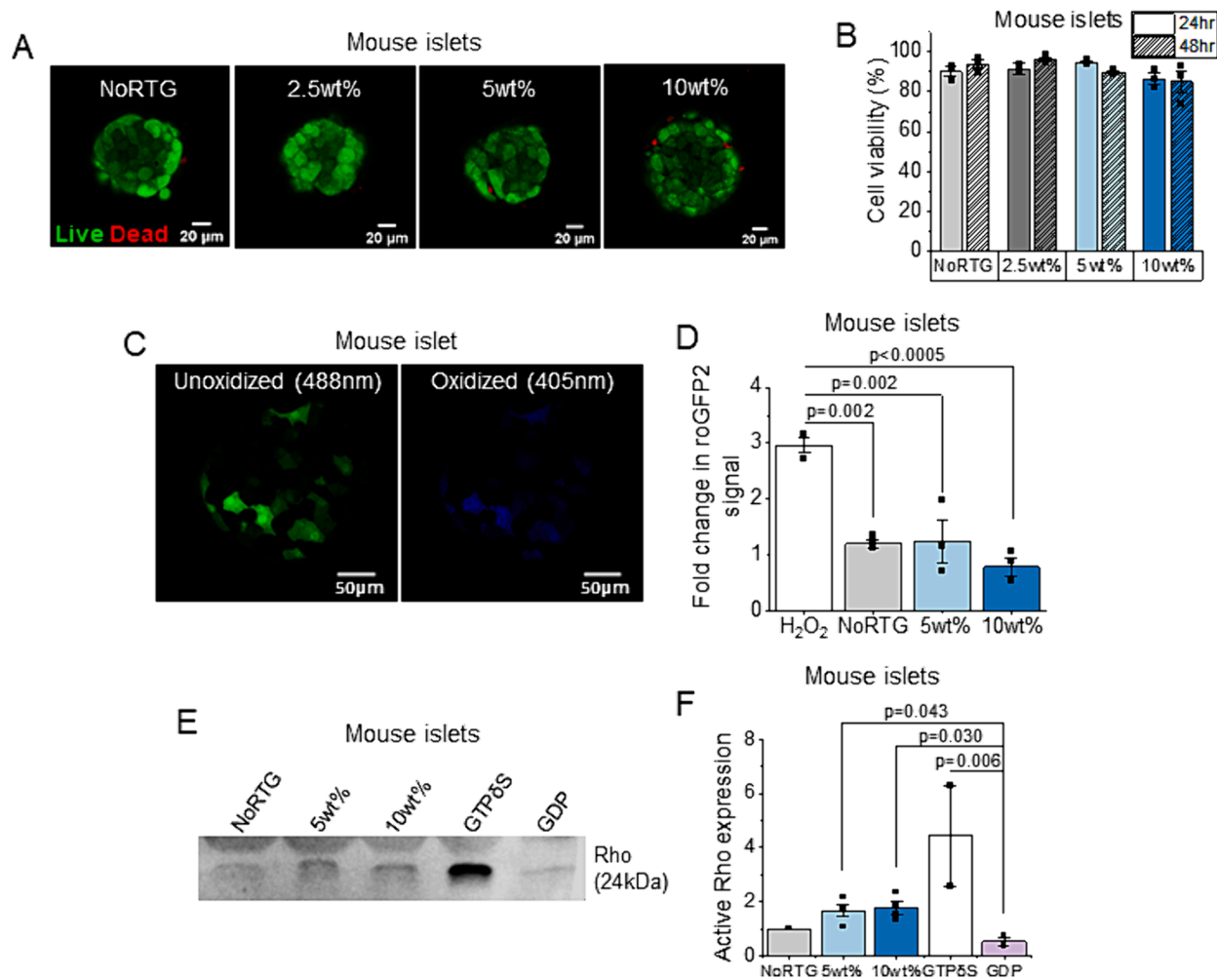
Fig. 3. Analysis of the RTG as a scaffold for islet culture and mechanotransduction interaction through focal adhesion formation. (A) Representative confocal microscopy images of mouse islet viability at 48hr where red represents dead cells stained with propidium iodide and green represents viable cells stained with fluorescein diacetate. (B) Viability data for mouse islets encapsulated in 2.5 wt%, 5 wt%, and 10 wt% RTG versus unencapsulated for 24 and 48-hr periods (n = 3). (C) Representative confocal microscopy images of the unoxidized (488 nm) and oxidized (405 nm) channels of the ROS sensor. (D) Analysis of reactive oxygen species using an adenoviral ROS sensor in 5 wt% and 10 wt% RTG encapsulated and unencapsulated mouse islets (n = 3). Data is presented as fold change in roGFP2 fluorescence intensity, calculated by dividing the fluorescence intensity of the oxidized state by the fluorescence intensity of the unoxidized state. Both channels were corrected to background prior to ratiometric calculation. (E) Representative western blot of Rho in whole mouse islets unencapsulated and encapsulated in 5 wt% and 10 wt% RTG treated with 11 mM glucose for 1hr (n = 4). GTPδS and GDP are the positive and negative controls, respectively. (F) Western blot quantification for Rho expression in mouse islets. Rho expression was normalized to total protein content via BCA assay. Error bars represent the mean +/- SEM. $p < 0.05$ indicates statistical significance as determine by ANOVA with Tukey's post hoc analysis. (For interpretation of the references to color in this figure legend, the reader is referred to the web version of this article.)

As GSIS is tightly coupled to ATP levels governed by glucose metabolism in the β-cell, we explored stiffness induced changes in glycolysis [27,50]. Given Piezo1's ability to regulate intracellular Ca^{2+} influx, we investigated changes in phosphofructokinase (PFK), which is subject to regulation by Ca^{2+} signaling and governs the activity of glucokinase—the rate-limiting step in glycolysis [26,29,51–53]. We determined if changes in PFK activity are associated with dysfunction to insulin secretion in islets encapsulated in stiff RTG. In mouse islets at 11 mM glucose, increasing RTG stiffness increased PFK activity when normalized to the NoRTG control (no inhibitor) condition (p = 0.033, Fig. 5F). Addition of GsMTx-4 in mouse islets causes a decrease in PFK activity in all conditions when normalized to the NoRTG control (no inhibitor) condition (Fig. 5F). Inhibition of Piezo1 via GsMTx-4 in 10 wt% RTG decreased PFK activity to similar levels as in the NoRTG control (p = 0.001, Fig. 5F). Overall, our results support a role for Piezo1 in regulating PFK activity in the β-cell.

To determine whether the dysfunction in GSIS observed in stiff RTG is attributed to Piezo1-mediated Ca^{2+} influx, we next analyzed

intracellular Ca^{2+} dynamics in islets encapsulated in RTG. In the NoRTG condition, we do not see active Ca^{2+} dynamics at basal, 2 mM glucose stimulation (Fig. 6A and Supplemental Video V1). After addition of 11 mM glucose there is a sudden elevation in intracellular Ca^{2+} characteristic of a 1st phase Ca^{2+} response followed by Ca^{2+} oscillations characteristic of a 2nd phase Ca^{2+} response [54]. A similar response was triggered by the addition of 20 mM glucose with a slight increase in amplitude of high frequency Ca^{2+} oscillations. Further, the addition of KCl completely depolarizes the cell membrane triggering a substantial increase in intracellular Ca^{2+}, providing evidence of normal K_{ATP} channel function [55,56]. In 2.5 wt% and 5 wt% RTG we see similar Ca^{2+} dynamics at 2 mM glucose to the NoRTG control (Fig. 6A-C). In the 5 wt% RTG we see a slightly diminished response to 20 mM glucose compared to the substantial jump in Ca^{2+} in the NoRTG condition (Fig. 6C). The 2.5 wt% and 5 wt% encapsulated islets responded to KCl stimulation similar to the NoRTG control. Quantification of the fraction of active islet area at 2 mM glucose further showed that the active islet fraction increased with increasing RTG stiffness/wt%, where the 10 wt%
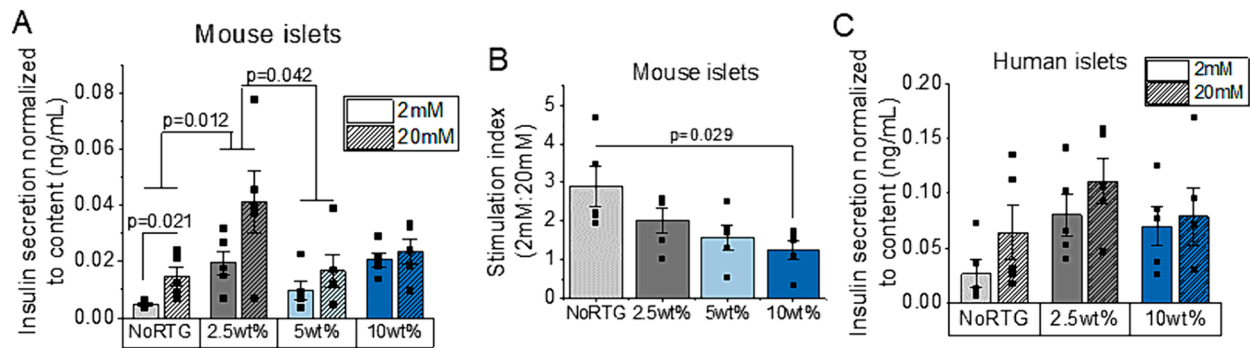
Fig. 4. Analysis of mouse and human islet function with changes in RTG stiffness. (A) Secreted insulin normalized to insulin content for mouse islets encapsulated in 2.5 wt%, 5 wt% and 10 wt% RTG or unencapsulated islets at non-stimulatory (2 mM) and stimulatory (20 mM) glucose concentrations (n = 4). (B) The stimulation index, or the ratio of insulin secretion at 20 mM glucose to 2 mM glucose, of the same treatment groups in A (n = 4). (C) Secreted insulin normalized to insulin content for human islets encapsulated in 2.5 wt% and 10 wt% RTG or unencapsulated islets at non-stimulatory (2 mM) and stimulatory (20 mM) glucose concentrations (n = 5). Error bars represent the mean +/- SEM. $p < 0.05$ indicates statistical significance as determine by ANOVA with Tukey's post hoc analysis.
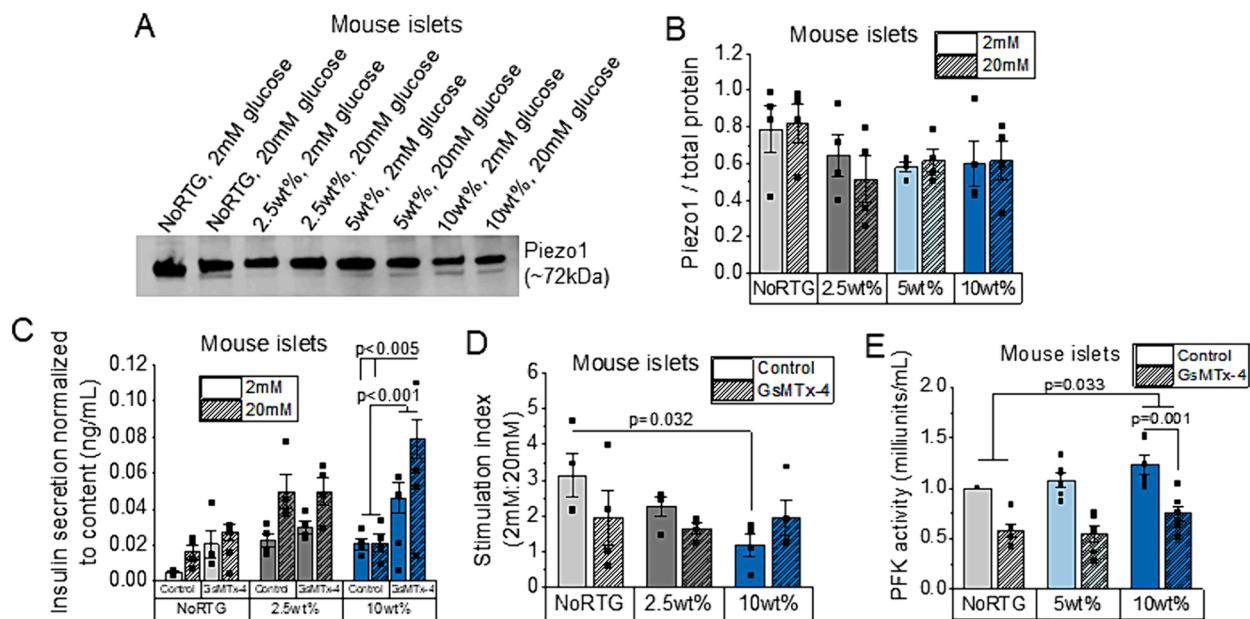

Fig. 5. Piezo1 localization and islet function analysis in mouse islets unencapsulated and encapsulated in RTG. (A) Representative western blot of Piezo1 in whole mouse islets unencapsulated and encapsulated in 2.5 wt%, 5 wt%, and 10 wt% RTG treated with 2 mM and 20 mM glucose for 1hr (n = 4). (B) Western blot quantification for Piezo1 expression in mouse islets. Piezo1 expression was normalized to total protein content via Ponceau staining and BCA assay. (C) GSIS with non-stimulatory (2 mM) and stimulatory (20 mM) glucose with (+) or without (-) the peptide inhibitor GsMTx-4 (2.5 μM) added to the glucose solution in 2.5 wt% and 10 wt% encapsulated or unencapsulated mouse islets (n = 4). (D) Stimulation index from 2 mM to 20 mM glucose with the GsMTx-4 inhibitor or the control as calculated from data in B (n = 4). (E) PFK activity, reported as milliunit/mL = nmole/min/mL, in 5 wt% or 10 wt% encapsulated or unencapsulated mouse islets treated with 11 mM glucose with the GsMTx-4 inhibitor or the control (n = 6). Data is normalized to the NoRTG control (no inhibition) condition. Error bars represent the mean +/- SEM. $p < 0.05$ indicates statistical significance as determine by ANOVA with Tukey's post hoc analysis.

RTG was significantly higher than the NoRTG condition (p = 0.048, Fig. 6J). The spike in Ca^{2+} at low glucose was primarily seen in cells that are closest to the islet periphery (Fig. 6E and Supplemental Video V2). As the expression of the GCaMP Ca^{2+} sensor is driven by the mouse insulin promotor, we can confirm that the cells on the periphery with increased basal Ca^{2+} are β-cells and not α-cells that would normally be active at low glucose [57]. The 2.5 wt% 1st phase AUC and the oscillation amplitude are increased over the NoRTG control (Fig. 6K, M). In stiff 10 wt% RTG, there is an increase in active cells triggering influx of Ca^{2+} at 2 mM glucose (Fig. 6D and Supplemental Video 2). The 10 wt% encapsulated islets showed a less pronounced 1st phase Ca^{2+} response, indicated by the decrease in the 1st phase AUC, although this was not statistically significant (Fig. 6K). Increasing RTG stiffness did not alter oscillation frequency under any of the conditions tested (Fig. 6L). The 10 wt% RTG islets also respond normally to KCl stimulation, like the

other conditions. The amplitude of the 11 mM glucose Ca^{2+} oscillations increased with increasing matrix stiffness when compared to the NoRTG control, where the 10 wt% RTG was significantly higher than the NoRTG condition (p = 0.020, Fig. 6M). Addition of the Piezo1 inhibitor GsMTx-4 seems to increase high frequency Ca^{2+} oscillations in all conditions compared to the control (no inhibitor) in both unencapsulated and RTG encapsulated islets as seen in our representative Ca^{2+} traces (Fig. 6F-I). GsMTx-4 treatment decreased the amplitude of the 1st phase 11 mM Ca^{2+} oscillations in all RTG encapsulated conditions compared to the RTG control samples. Specifically, the 2.5 wt% RTG sample with GsMTx-4 was significantly lower than the 2.5 wt% RTG control (p = 0.017, Fig. 6M). The addition of GsMTx-4 in the 5 and 10 wt% RTG condition slightly increased the 1st phase AUC compared to the RTG control sample (Fig. 6K-L). Moreover, GsMTx-4 abolished the 2 mM glucose oscillations in the 10 wt% encapsulated islets (Fig. 6I). The fraction of
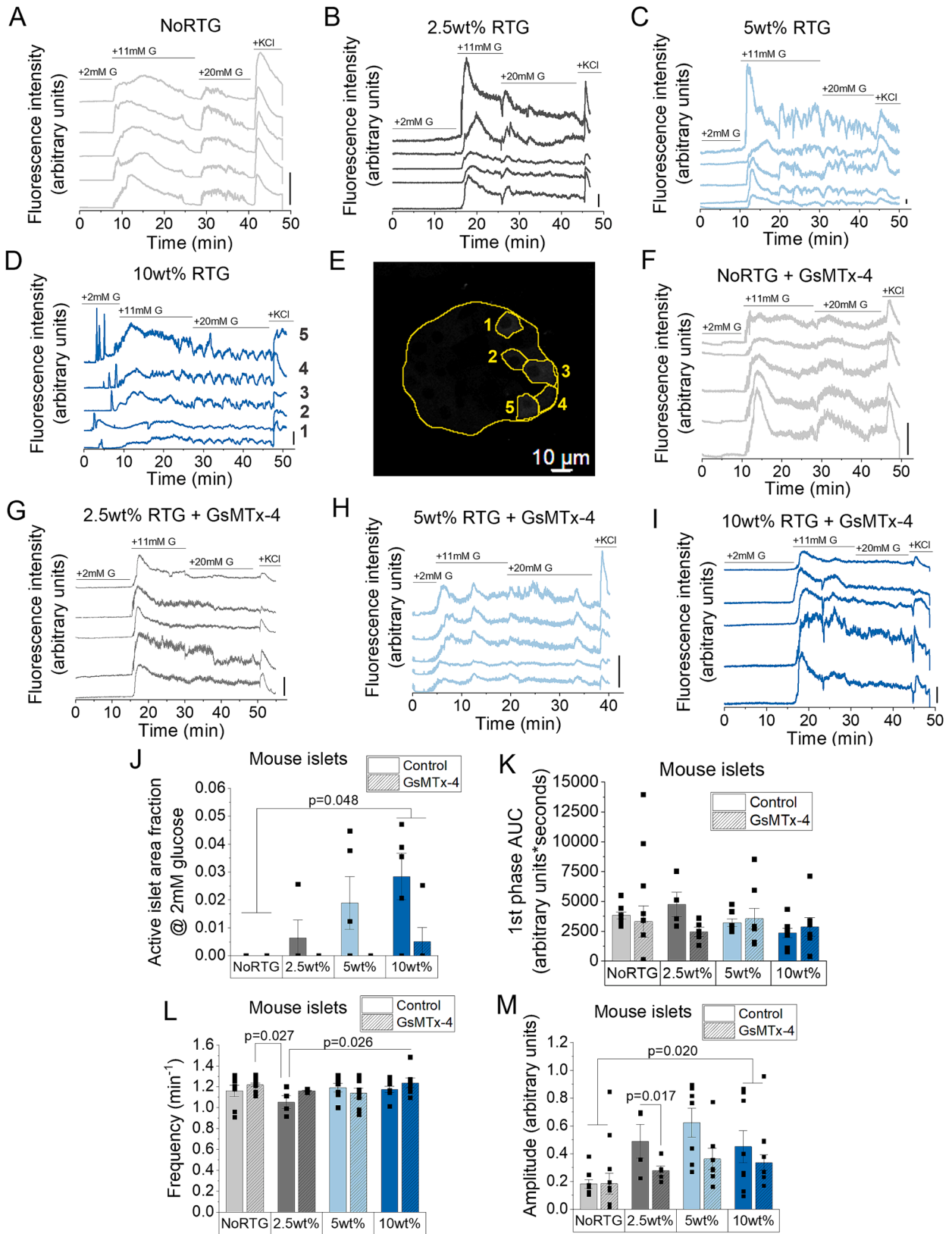
(caption on next page)

Fig. 6. Ca^{2+} analysis of mouse islets with changes in RTG stiffness. Representative traces of intracellular Ca^{2+} as measured by fluorescence intensity in 5 individual cells in the same islet over time in islets (A) unencapsulated, or encapsulated in (B) 2.5 wt% RTG, (C) 5 wt% RTG, and (D) 10 wt% RTG. Bars indicate a 900 % change in Ca^{2+} compared with the baseline Ca^{2+} levels. (E) Representative image of a mouse islet encapsulated in 10 wt% RTG treated with 2 mM glucose. The yellow outlined cells were oscillating at low glucose and are numbered according to corresponding Ca^{2+} trace in Fig. 6D. Representative traces of intracellular Ca^{2+} as measured by fluorescence intensity in 5 individual cells in the same islet treated with the Piezo1 inhibitor GsMTx-4 (2.5 μM) over time in islets (F) unencapsulated, or encapsulated in (G) 2.5 wt% RTG, (H) 5 wt% RTG, and (I) 10 wt% RTG. Bars indicate a 900 % change in Ca^{2+} compared with the baseline Ca^{2+} levels. (J) Area fraction of active cells at 2 mM glucose to total islet area quantified in unencapsulated islets or islets encapsulated in 2.5 wt%, 5 wt%, or 10 wt% RTG treated with the GsMTx-4 inhibitor (2.5 μM) or the control (n = 3). (K) Area under the curve (AUC) of the 1st phase 11 mM glucose oscillation in unencapsulated islets or islets encapsulated in 2.5 wt%, 5 wt%, or 10 wt% RTG treated with the GsMTx-4 inhibitor (2.5 μM) or the control. Each data point represents a single islet (n = 4–8 islets, n = 3 mice). (L) Ca^{2+} oscillation frequency during 11 mM glucose stimulation in unencapsulated islets or islets encapsulated in 2.5 wt%, 5 wt%, or 10 wt% RTG treated with the GsMTx-4 inhibitor (2.5 μM) or the control. Each data point represents a single islet (n = 6–12 islets, n = 3 mice). (M) Amplitude of Ca^{2+} oscillations in unencapsulated islets or islets encapsulated in 2.5 wt%, 5 wt%, or 10 wt% RTG treated with the GsMTx-4 inhibitor (2.5 μM) or the control. Each data point represents a single islet (n = 6–12 islets, n = 3 mice). Error bars represent the mean +/- SEM. p < 0.05 indicates statistical significance as determine by ANOVA with Tukey's post hoc analysis. (For interpretation of the references to color in this figure legend, the reader is referred to the web version of this article.)

active islet area at 2 mM glucose in 10 wt% RTG drops significantly (p = 0.048, Fig. 6J). Overall, our results support a role for Piezo1 in mediating stiffness-induced dysfunction to insulin secretion regulation of Ca^{2+} dynamics.

Discussion

The goal of this study is to determine the role of Piezo1 in mediating stiffness-induced changes in islet function and insulin secretion. We hypothesized that increasing matrix stiffness will cause insulin secretion dysfunction by opening the mechanosensitive ion channel Piezo1 and disrupting intracellular Ca^{2+} dynamics. In this study we employed a biomimetic RTG encapsulation system to enable precise manipulation of mechanical stiffness of the islet microenvironment. Our results confirm that increased scaffold stiffness impairs GSIS through Piezo1-mediated mechanotransduction, disrupting Ca^{2+} dynamics and insulin secretion in both mouse and human islets (Fig. 7). Inhibiting Piezo1 via addition of GsMTx-4 in islets within a stiff scaffold rescues GSIS function and Ca^{2+} dynamics, underscoring Piezo1's role in regulating islet response to mechanical cues and contributing to insulin secretion dysfunction in stiff scaffolds. Understanding cellular signaling pathways that govern the

influence of mechanical cues on β-cell function informs the design of improved islet transplantation scaffolds, contributing to optimizing conditions for successful transplantation. Moreover, it aids in our understanding of islet function restoration in conditions like T2D and pancreatic cancer, where *peri*-islet ECM fibrosis leads to increased tissue stiffness and islet dysfunction.

RTG supports islet function and transmits mechanical cues via focal adhesions

To determine suitability of RTG for islet culture and investigation of mechanotransduction signaling, we characterized islet survival, stress, and formation of focal adhesions within a 3D RTG scaffold. PSHU-PNIPAAm RTG was chosen as our scaffold due to its ability to encapsulate islets under physiological conditions, its tunable mechanical properties, its biocompatibility, and its biomimetic nature [58–61]. Although it is fully synthetic, it mimics naturally occurring ECM biomolecules like heparan sulfate, which undergoes a phase change from solution to gel to aid in blood coagulation for wound healing purposes [62]. Similarly, the RTG undergoes a temperature dependent sol–gel transition, mediated by the PNIPAAm co-block, that can be reversed for
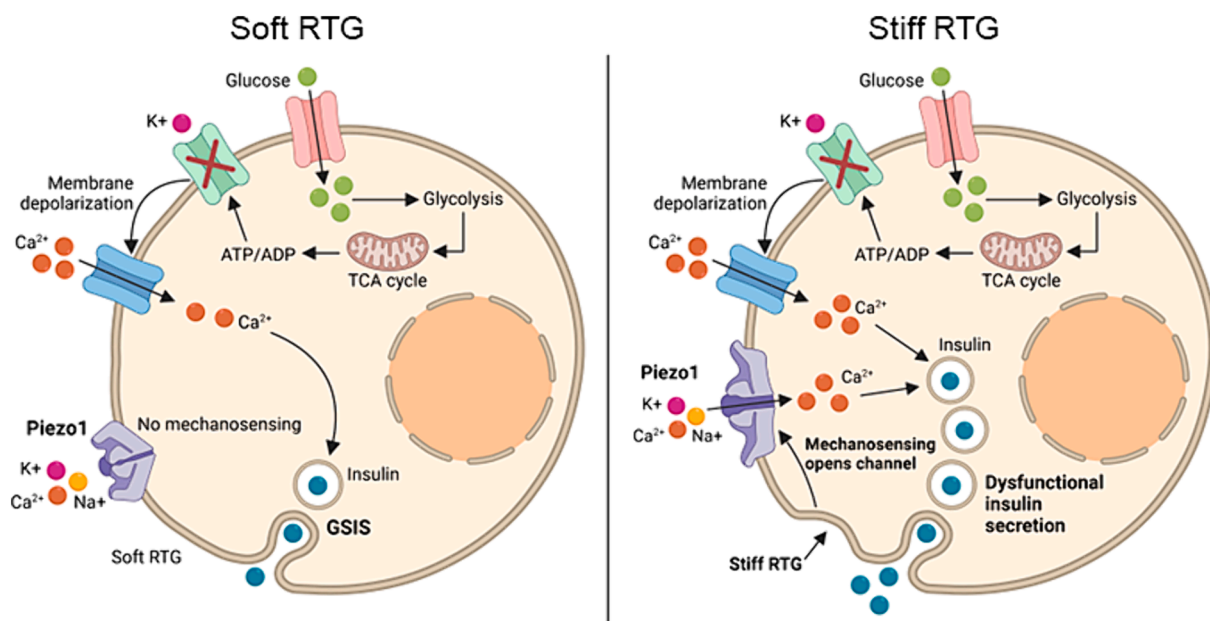

Fig. 7. Piezo1 mediates stiffness induced changes in islet insulin secretion via mechanotransduction with glucose stimulation. In soft matrices GSIS proceeds via the canonical pathway where glucose is taken up by the cell and metabolized into ATP via PFK activity, which yields an increase in the ATP/ADP ratio. This increase in ATP closes the ATP sensitive K$^+$ channels which causes membrane depolarization that opens voltage-gated Ca^{2+} channels and results in an intracellular flux of Ca^{2+} that triggers the release of insulin granules. In stiff matrices, forces transferred from the scaffold to the cell membrane open the non-specific cation channel Piezo1, allowing an influx of Ca^{2+} into the cell and dysfunction to insulin secretion at 2 mM and 20 mM glucose. The results from this study and our proposed mechanism supports a role for Piezo1 in regulating islet response to mechanical cues, leading to increased insulin release.

facile retrieval of encapsulated islets [32]. The structure of the RTG with pores and sheets significantly smaller than an islet ensures complete islet encapsulation while allowing nutrient flow in and out of the encapsulation system. This is supported by the high viability of encapsulated islets over time and the high level of diffusivity of both small and large molecules within the RTG. Further, our data demonstrates tunability of storage modulus, or stiffness, by varying RTG wt% where we achieved a range of 0.047–2.65 kPa for 2.5-15 wt% scaffolds. Although the storage modulus of 2.5 wt% RTG does not signifcantly increase upon temperature stimulus, it did undergo a change in opacity as proof of phase transition.

Previous studies utilizing islets encapsulated in non-reversible polymeric scaffolds have demonstrated islet damage due to the encapsulation process combined with low oxygen and nutrient diffusion into the scaffold that was characterized by the release of DAMPs from islet cells [63]. Our results indicate that islet encapsulation in RTG does not cause significant DAMP release as determined by ROS production in RTG encapsulated islets, suggesting that encapsulation in RTG does not cause islet damage or stress. Additionally, although our RTG is fully synthetic, our results indicate an increase in integrin interactions when mouse islets are encapsulated in RTG compared to the unencapsulated control, supporting the formation of focal adhesions with the RTG scaffold, and confirming the transduction of mechanical forces, like stiffness, from the scaffold to the encapsulated islet. This not only affirms our ability to examine the impact of RTG stiffness on islet function but also emphasizes its suitability for culturing encapsulated islets without compromising their functionality.

Increased scaffold stiffness causes dysfunction to GSIS via changes in Ca^{2+} dynamics

To determine if scaffold stiffness leads to insulin secretion dysfunction we analyzed GSIS and Ca^{2+} dynamics at 2 mM glucose, where we expect low basal levels of insulin secretion and no Ca^{2+} influx, and 20 mM glucose where we expect maximal glucose stimulated insulin secretion and a biphasic influx of Ca^{2+} [28,64]. Normal islet function was observed in unencapsulated mouse islets where insulin secretion at 20 mM glucose was 2.89-fold higher compared to basal 2 mM glucose. The observed enhancement in GSIS and the increase in Ca^{2+} activity, indicated by 1st phase Ca^{2+} AUC and amplitude, in islets encapsulated in 2.5 wt% RTG indicates improved islet function, aligning with previous studies demonstrating enhanced cell viability and function in PSHU-PNIPAAm scaffolds [33,39,41]. As matrix stiffness increases, islet dysfunction to insulin secretion occurs at both 2 mM and 20 mM glucose, as illustrated by the decrease in decrease in stimulation index, which is similar to the loss of GSIS observed in T2D where fibrosis of the *peri*-islet ECM leads to increased tissue stiffness and islet dysfunction [10,65]. This is further supported by our Ca^{2+} data where we observed a less pronounced 1st phase Ca^{2+} response and a loss of Ca^{2+} oscillations at 11 mM and 20 mM glucose that may contribute to decreases in GSIS [66]. While the impaired insulin secretion in stiff RTGs aligns with phenotypic models of altered K_{ATP} channel function, our Ca^{2+} data in response to KCl stimulation suggests that K_{ATP} channels are not altered as stiffness increases [67]. We observed high levels of coordination of islet Ca^{2+} oscillations in all of our experimental conditions, suggesting that gap junction coupling is not disrupted and does not contribute to altered islet function [68]. Our findings indicate that the frequency of Ca^{2+} oscillations remained relatively stable across all tested conditions which is supported by literature where oscillation frequency does not change in T2D and also suggests normal function of the islet K_{ATP} channels despite increasing stiffness [69–71]. The observed effects of matrix stiffness on dysfunction to GSIS were primarily attributed to a slight decrease in AUC of the 1st phase of Ca^{2+} signaling dynamics. The increase in Ca^{2+} oscillation amplitude with increasing matrix stiffness further supports Piezo1 contributions to alterations in Ca^{2+} signaling dynamics, where stiffness induced opening of Piezo1 channels may contribute to this

observed increase in Ca^{2+}. While changes in RTG properties may still account for a portion of the reduced GSIS at 20 mM glucose, our data strongly supports that altered GSIS is attributed to mechanosensing of increased RTG stiffness and not altered diffusivity in the scaffold or permeability of insulin through the RTG as insulin secretion measurements included insulin secreted to both the surrounding media and the RTG scaffold.

Mouse islets encapsulated in stiff 10 wt% RTG also showed increased insulin secretion and Ca^{2+} activity at 2 mM glucose stimulation. This may represent a shift in the range of glucose responsiveness of the islet, which is normally confined by islet electrical activity, and likely contributes to the increase in insulin secretion observed at 2 mM glucose in 10 wt% RTG [72]. Additionally, the spike in Ca^{2+} at low glucose is most frequently observed in β-cells that are closest to the islet periphery, where Piezo1 was localized and where mechanotransduction signaling likely originates in the 3D structure of the islet. Combined, our data supports the transduction of mechanical stiffness from the RTG to the islet periphery via Piezo1 activation and further transduction of the signaling cascade via intracellular Ca^{2+} dynamics and membrane polarization to the internal islet β-cells which are physically and electrically coupled to the peripheral cells by gap junctions [73,74]. Overall, our findings indicate that altered Ca^{2+} dynamics regulated by increased matrix stiffness mediate islet dysfunction to GSIS and support a role for Piezo1 in mediating the islet response to scaffold stiffness.

Piezo1 mediates stiffness induced islet dysfunction

Previous data has shown that Piezo1 colocalizes with focal adhesions on the plasmas membrane that promote adhesion dynamics through force-dependent Ca^{2+} signaling [75]. This is consistent with our results where Piezo1 expression was shown under both soft and stiff RTG conditions and increased Ca^{2+} activity at low glucose was localized to the peripheral cells facing the RTG scaffold. Piezo1 activation has also been shown to be upregulated with increased matrix stiffness in other cell types [76]. Similarly, our results showed increased Ca^{2+} influx at low glucose in stiff RTG. Given our understanding of Piezo1 co-localization with focal adhesions, this further supports that mechanical cues evident on the periphery of the islet are capable of intracellular transduction via Piezo1. Inhibition of Piezo1 in stiff matrices abolished Ca^{2+} activity at 2 mM glucose, improved glucose-stimulated Ca^{2+} oscillations, and rescued insulin secretion as measured by SI. It was also observed that upon Piezo1 inhibition, Ca^{2+} oscillation amplitude decreased in our stiff 10 wt% RTG condition, further supporting a role for Piezo1-mediated Ca^{2+} influx in stiff RTGs contributing to altered Ca^{2+} dynamics. Altogether, this strongly supports a role for Piezo1 mediated Ca^{2+} influx in driving dysfunction to GSIS in intact islets encapsulated in stiff scaffolds.

GSIS is also regulated by metabolic cell signaling events within glycolysis, particularly activation of PFK, which regulates the rate-limiting step glucokinase and has been shown to be regulated by changes in intracellular Ca^{2+} [53,77,78]. Our results showing increased PFK activity with increased RTG stiffness are aligned with results in other cells types and support a potential role for altered glycolysis rates in contributing to increases in insulin secretion at low glucose as increased rates of glycolysis mediate membrane depolarization and insulin exocytosis [79]. Additionally, inhibiting Piezo1 in mouse islets encapsulated in stiff RTG decreased PFK activity. These results suggest that mechanotransduction by the Piezo1 channel may also regulate islet metabolism that could contribute to altered insulin secretion. Previous studies in other cell types show Piezo1 closure boosts ATP production and promotes glycolysis and that altered intracellular Ca^{2+} may regulate the activity of PFK [53,79]. While outside of the scope of the current work, future studies will determine if Piezo1 regulates the islet response to mechanical cues through Ca^{2+}-mediated upregulation PFK activity and dysfunctional GSIS.

Conclusions

In conclusion, we utilized a biomimetic RTG encapsulation system to investigate how changes in scaffold stiffness impact islet function and the role of Piezo1. We found that RTG scaffolds can form focal adhesions with encapsulated islets and that Piezo1 expression in the islet transduces mechanical cues throughout the islet via intracellular Ca^{2+} influx. Our results confirm that increased scaffold stiffness impairs GSIS through Piezo1-mediated mechanotransduction, disrupting Ca^{2+} dynamics and insulin secretion in both mouse and human islets. Furthermore, inhibiting Piezo1 within a stiff scaffold rescued GSIS and Ca^{2+} dynamics, emphasizing Piezo1′s role in regulating islet response to mechanical cues and contributing to insulin secretion dysfunction in stiff scaffolds. Understanding cellular signaling pathways that govern the influence of mechanical cues on β-cell function will inform the development of novel therapies to restore islet function in pancreatic diseases like T2D and pancreatic cancer.

Funding

CRediT authorship contribution statement

Chelsea G. Johansen: Writing – review & editing, Writing – original draft, Methodology, Formal analysis, Data curation, Conceptualization. **Keifer Holcomb:** Formal analysis, Data curation. **Amit Sela:** Formal analysis, Data curation. **Stephanie Morrall:** Formal analysis, Data curation. **Daewon Park:** Writing – review & editing, Resources, Conceptualization. **Nikki L. Farnsworth:** Writing – review & editing, Writing – original draft, Validation, Supervision, Project administration, Methodology, Investigation, Funding acquisition, Formal analysis, Conceptualization.

Declaration of competing interest

The authors declare that they have no known competing financial interests or personal relationships that could have appeared to influence the work reported in this paper.

Data availability

Data will be made available on request.

Appendix A. Supplementary data

Supplementary data to this article can be found online at https://doi.org/10.1016/j.mbplus.2024.100148.

References

[1] G. Da, S. Xavier, The Cells of the Islets of Langerhans. (2018) 1–17, https://doi.org/10.3390/jcm7030054.

[2] J.C. Stendahl, D.B. Kaufman, S.I. Stupp, Extracellular Matrix in Pancreatic Islets: Relevance to Scaffold Design and Transplantation, Cell Transplant. 18 (1) (2009) 1–12, https://doi.org/10.3727/096368909788237195.

[3] M. Bogdani, C. Speake, M.J. Dufort, P.Y. Johnson, M.J. Larmore, A.J. Day, T.N. Wight, Å. Lernmark, C.J. Greenbaum, Hyaluronan deposition in islets may precede and direct the location of islet immune-cell infiltrates, Diabetologia 63 (3) (2020) 549–560, https://doi.org/10.1007/s00125-019-05066-7.

[4] P.L. Bollyky, M. Bogdani, J.B. Bollyky, R.L. Hull, T.N. Wight, The role of hyaluronan and the extracellular matrix in islet inflammation and immune regulation, Curr. Diab. Rep. 12 (5) (2012) 471–480, https://doi.org/10.1007/s11892-012-0297-0.

[5] G. Alessandra, M. Algerta, M. Paola, S. Carsten, L. Cristina, M. Paolo, T. Gabriella, P. Carla, Shaping pancreatic B-cell differentiation and functioning : the influence of mechanotransduction, Cells 9 (413) (2020) 1–24.

[6] C.E. Nyitray, M.G. Chavez, T.A. Desai, Compliant 3D microenvironment improves β-cell cluster insulin expression through mechanosensing and β-catenin signaling, Tissue Eng. A 20 (13–14) (2014) 1888–1895, https://doi.org/10.1089/ten.tea.2013.0692.

[7] W. Zhang, S. Zhang, W. Zhang, Y. Yue, W. Qian, Z. Wang, Matrix stiffness and its influence on pancreatic diseases, Biochim. Biophys. Acta 1876 (1) (2021) 188583, https://doi.org/10.1016/j.bbcan.2021.188583.

[8] S.C. Wei, L. Fattet, J.H. Tsai, Y. Guo, V.H. Pai, H.E. Majeski, A.C. Chen, R.L. Sah, S.S. Taylor, J. Adam, Matrix Stiffness Drives Epithelial-Mesenchymal Transition and Tumour Metastasis through a TWIST1-G3BP2 Mechanotransduction Pathway. 17 (5) (2015) 678–688, https://doi.org/10.1038/ncb3157.Matrix.

[9] D. Thomas, P. Radhakrishnan, Tumor-stromal crosstalk in pancreatic cancer and tissue fibrosis, Mol. Cancer 18 (1) (2019) 1–15, https://doi.org/10.1186/s12943-018-0927-5.

[10] R.L. Hull, G.T. Westermark, P. Westermark, S.E. Kahn, Islet amyloid: a critical entity in the pathogenesis of type 2 diabetes, J. Clin. Endocrinol. Metab. 89 (8) (2004) 3629–3643, https://doi.org/10.1210/jc.2004-0405.

[11] A.S. Williams, L. Kang, D.H. Wasserman, The extracellular matrix and insulin resistance, Trends Endocrinol. Metab. 26 (7) (2015) 357–366, https://doi.org/10.1016/j.tem.2015.05.006.

[12] D. Lin, T.H. Chun, L. Kang, Adipose extracellular matrix remodelling in obesity and insulin resistance, Biochem. Pharmacol. 119 (2016) 8–16, https://doi.org/10.1016/j.bcp.2016.05.005.

[13] N. Nagy, A. de la Zerda, G. Kaber, P.Y. Johnson, K.H. Hu, M.J. Kratochvil, K. Yadava, W. Zhao, Y. Cui, G. Navarro, J.P. Annes, T.N. Wight, S.C. Heilshorn, P.L. Bollyky, M.J. Butte, Hyaluronan content governs tissue stiffness in pancreatic islet inflammation, J. Biol. Chem. 293 (2) (2018) 567–578, https://doi.org/10.1074/jbc.RA117.000148.

[14] S. Calderari, J. Irminger, J. Coulaud, K. Rickenbach, M. Dolz, P. Halban, B. Portha, P. Serradas, Islet inflammation and fibrosis in a spontaneous model of type 2 diabetes, the GK rat, Diabetes 55 (2006), https://doi.org/10.2337/db05-1526.

[15] V.M. Perez, J.F. Kearney, J.J. Yeh, The PDAC extracellular matrix: a review of the ECM protein composition, tumor cell interaction, and therapeutic strategies, Front. Oncol. 11 (October) (2021) 1–10, https://doi.org/10.3389/fonc.2021.751311.

[16] P. Zhao, T. Sun, C. Lyu, K. Liang, Y. Du, Cell mediated ECM – degradation as an emerging tool for anti-fibrotic strategy, Cell Regeneration 12 (29) (2023) 1–16, https://doi.org/10.1186/s13619-023-00172-9.

[17] Rubis, M.; Secq, V.; Moutardier, V.; Lombardo, D.; Iovanna, J. L.; Tomasini, R.; Guillaumond, F.; Heiden, M. G. Vander; Vasseur, S. Collagen-Derived Proline Promotes Pancreatic Ductal Adenocarcinoma Cell Survival under Nutrient Limited Conditions. *Nat Commun* **2017**, No. May. https://doi.org/10.1038/ncomms16031.

[18] T. Armstrong, G. Packham, L.B. Murphy, A.C. Bateman, J.A. Conti, D.R. Fine, C.D. Johnson, R.C. Benyon, J.P. Iredale, Type I collagen promotes the malignant phenotype of pancreatic ductal adenocarcinoma, Clin. Cancer Res. 10 (2004) 7427–7437.

[19] A.J. Rice, E. Cortes, D. Lachowski, B.C.H. Cheung, S.A. Karim, J.P. Morton, A. Del Río Hernández, Matrix stiffness induces epithelial-mesenchymal transition and promotes chemoresistance in pancreatic cancer cells, Oncogenesis 6 (7) (2017) 1–9, https://doi.org/10.1038/oncsis.2017.54.

[20] M. Bogdani, P.Y. Johnson, S. Potter-Perigo, N. Nagy, A.J. Day, P.L. Bollyky, T.N. Wight, Hyaluronan and hyaluronan-binding proteins accumulate in both human type 1 diabetic islets and lymphoid tissues and associate with inflammatory cells in insulitis, Diabetes 63 (8) (2014) 2727–2743, https://doi.org/10.2337/db13-1658.

[21] C. Arous, B. Wehrle-Haller, Role and impact of the extracellular matrix on integrin-mediated pancreatic β-cell functions, Biol. Cell 109 (6) (2017) 223–237, https://doi.org/10.1111/boc.201600076.

[22] E.B. Hammar, J.C. Irminger, K. Rickenbach, G. Parnaud, P. Ribaux, D. Bosco, D.G. Rouiller, P.A. Halban, Activation of NF-KB by extracellular matrix is involved in spreading and glucose-stimulated insulin secretion of pancreatic beta cells, J. Biol. Chem. 280 (34) (2005) 30630–30637, https://doi.org/10.1074/jbc.M502493200.

[23] A. Galli, E. Maffioli, E. Sogne, S. Moretti, E.S. Di Cairano, A. Negri, S. Nonnis, G.D. Norata, F. Bonacina, F. Borghi, A. Podestà, F. Bertuzzi, P. Milani, C. Lenardi, G. Tedeschi, C. Perego, Cluster-assembled zirconia substrates promote long-term differentiation and functioning of human islets of langerhans, Sci. Rep. 8 (1) (2018) 1–17, https://doi.org/10.1038/s41598-018-28019-3.

[24] S.H. Kim, J. Turnbull, S. Guimond, Extracellular matrix and cell signalling: the dynamic cooperation of integrin, proteoglycan and growth factor receptor, J. Endocrinol. 209 (2) (2011) 139–151, https://doi.org/10.1530/JOE-10-0377.

[25] B. Yang, K. Wei, C. Loebel, K. Zhang, Q. Feng, R. Li, S.H.D. Wong, X. Xu, C. Lau, X. Chen, P. Zhao, C. Yin, J.A. Burdick, Y. Wang, L. Bian, Enhanced mechanosensing of cells in synthetic 3D matrix with controlled biophysical dynamics, Nat. Commun. 12 (1) (2021), https://doi.org/10.1038/s41467-021-23120-0.

[26] V. Deivasikamani, S. Dhayalan, Y. Abudushalamu, R. Mughal, A. Visnagri, K. Cuthbertson, J.L. Scragg, T.S. Munsey, H. Viswambharan, K. Muraki, R. Foster, A. Sivaprasadarao, M.T. Kearney, D.J. Beech, P. Sukumar, Piezo1 channel activation mimics high glucose as a stimulator of insulin release, Sci. Rep. 9 (1) (2019) 1–10, https://doi.org/10.1038/s41598-019-51518-w.

[27] J. Henquin, Triggering and amplifying pathways of regulation of insulin secretion by, Glucose. (1751).

[28] J. Henquin, N. Ishiyama, M. Nenquin, M.A. Ravier, Jonas J. Signals and Pools Underlying Biphasic Insulin Secretion. 51 (2002).

[29] Y. Ye, M. Barghouth, H. Dou, C. Luan, Y. Wang, A. Karagiannopoulos, X. Jiang, U. Krus, M. Fex, Q. Zhang, L. Eliasson, P. Rorsman, E. Zhang, E. Renström, A Critical Role of the Mechanosensor PIEZO1 in Glucose-Induced Insulin Secretion in Pancreatic Beta, Cells. (2022) 1–16, https://doi.org/10.1038/s41467-022-31103-y.

[30] H. Liu, J. Hu, Q. Zheng, X. Feng, F. Zhan, X. Wang, G. Xu, F. Hua, Piezo1 channels as force sensors in mechanical force-related chronic inflammation, Front. Immunol. 13 (January) (2022) 1–20, https://doi.org/10.3389/fimmu.2022.816149.

[31] Wang, B.; Ke, W.; Wang, K.; Li, G.; Ma, L.; Lu, S.; Xiang, Q.; Liao, Z.; Luo, R.; Song, Y.; Hua, W.; Wu, X.; Zhang, Y.; Zeng, X.; Yang, C. Mechanosensitive Ion Channel Piezo1 Activated by Matrix Stiffness Regulates Oxidative Stress-Induced Senescence and Apoptosis in Human Intervertebral Disc Degeneration. *Oxid Med Cell Longev* **2021**, *2021*. https://doi.org/10.1155/2021/8884922.

[32] R. Shandas, D. Park, A Heparin-Mimicking Reverse Thermal Gel for Controlled Delivery of Positively Charged Proteins. 103 (6) (2016) 2102–2108, https://doi.org/10.1002/jbm.a.35345.A.

[33] B. Peña, V. Martinelli, M. Jeong, S. Bosi, R. Lapasin, M.R.G. Taylor, C.S. Long, R. Shandas, D. Park, L. Mestroni, Biomimetic polymers for cardiac tissue engineering, Biomacromolecules 17 (5) (2016) 1593–1601, https://doi.org/10.1021/acs.biomac.5b01734.

[34] M. Kang, C.A. Day, A.K. Kenworthy, E. DiBenedetto, Simplified equation to extract diffusion coefficients from confocal FRAP data, Traffic 13 (12) (2012) 1589–1600, https://doi.org/10.1111/tra.12008.Simplified.

[35] C.A. Reissaus, A.R. Piñeros, A.N. Twigg, K.S. Orr, A.M. Conteh, M.M. Martinez, M. M. Kamocka, R.N. Day, S.A. Tersey, R.G. Mirmira, K.W. Dunn, A.K. Linnemann, A versatile, portable intravital microscopy platform for studying beta-cell biology in vivo, Sci. Rep. 9 (1) (2019) 1–11, https://doi.org/10.1038/s41598-019-44777-0.

[36] V. Kravets, J.A.M. Dwulet, W.E. Schleicher, D.J. Hodson, A.M. Davis, L. Pyle, R. A. Piscopio, M. Sticco-Ivins, R.K.P. Benninger, Functional architecture of pancreatic islets identifies a population of first responder cells that drive the first-phase calcium response, PLoS Biol. 20 (9) (2022) 1–25, https://doi.org/10.1371/journal.pbio.3001761.

[37] Morrall, S.; Farnsworth, N. L. *s-morrall/Calcium-Analysis*. https://github.com/s-morrall/Caluicium-Analysis.

[38] C.H. Emfinger, L.E. Clark, B. Yandell, K.L. Schueler, S.P. Simonett, D.S. Stapleton, K.A. Mitok, M.J. Merrins, M.P. Keller, A.D. Attie, Novel regulators of islet function identified from genetic variation in mouse islet Ca2+ oscillations, Elife 12 (2023) 1–28, https://doi.org/10.7554/eLife.88189.1.

[39] A. Famili, M.Y. Kahook, D. Park, A combined micelle and poly(serinol hexamethylene urea)-co-poly(N-Isopropylacrylamide) reverse thermal gel as an injectable ocular drug delivery system, Macromol. Biosci. 14 (12) (2014) 1719–1729, https://doi.org/10.1002/mabi.201400250.

[40] D. Park, V. Shah, B.M. Rauck, T.R. Friberg, Y. Wang, An anti-angiogenic reverse thermal gel as a drug-delivery system for age-related wet macular degeneration, Macromol. Biosci. 13 (4) (2013) 464–469, https://doi.org/10.1002/mabi.201200384.

[41] J. Bardill, S.M. Williams, U. Shabeka, L. Niswander, D. Park, A.I. Marwan, An injectable reverse thermal gel for minimally invasive coverage of mouse myelomeningocele, J. Surg. Res. 235 (2019) 227–236, https://doi.org/10.1016/j.jss.2018.09.078.

[42] D.S.A. Simpson, P.L. Oliver, ROS generation in microglia: understanding oxidative stress and inflammation in neurodegenerative disease, Antioxidants 9 (8) (2020) 1–27, https://doi.org/10.3390/antiox9080743.

[43] H. Nakano, S. Murai, K. Moriwaki, Regulation of the release of damage-associated molecular patterns from necroptotic cells, Biochem. J 479 (5) (2022) 677–685, https://doi.org/10.1042/BCJ20210604.

[44] S. Huveneers, E.H.J. Danen, Adhesion signaling - crosstalk between integrins, Src and Rho. *J Cell Sci* 122 (8) (2009) 1059–1069, https://doi.org/10.1242/jcs.039446.

[45] P. Kanchanawong, D.A. Calderwood, Organization, dynamics and mechanoregulation of integrin-mediated Cell–ECM adhesions, Nat. Rev. Mol. Cell Biol. 24 (2) (2023) 142–161, https://doi.org/10.1038/s41580-022-00531-5.

[46] J. Schrader, T.T. Gordon-Walker, R.L. Aucott, M. van Deemter, A. Quaas, S. Walsh, D. Benten, S.J. Forbes, R.G. Wells, J.P. Iredale, Matrix stiffness modulates proliferation, chemotherapeutic response, and dormancy in hepatocellular carcinoma cells, Hepatology 53 (4) (2011) 1192–1205, https://doi.org/10.1002/hep.24108.

[47] Y.T. Yeh, S.S. Hur, J. Chang, K.C. Wang, J.J. Chiu, Y.S. Li, S. Chien, Matrix stiffness regulates endothelial cell proliferation through septin 9, PLoS One 7 (10) (2012) 1–13, https://doi.org/10.1371/journal.pone.0046889.

[48] Morris et al., 2012; et al., 2012. The Mechanosensitive Ion Channel Piezo1 Is Inhibited by the Peptide GsMTx4. *Gerontology* **2015**, *61* (6), 515–525. https://doi.org/10.1021/bi200770q.The.

[49] Qiu, Z.; Chan, C.; Qiu, Z.; Guo, J.; Kala, S.; Zhu, J.; Xian, Q.; Qiu, W.; Li, G. The Mechanosensitive Ion Channel Piezo1 Significantly Mediates In Vitro Ultrasonic Stimulation of Neurons The Mechanosensitive Ion Channel Piezo1 Significantly Mediates In Vitro Ultrasonic Stimulation of Neurons. *iScience* **2019**, *21*, 448–457. https://doi.org/10.1016/j.isci.2019.10.037.

[50] S. Lenzen, A Fresh View of Glycolysis and Glucokinase Regulation : History and Current Status *, J. Biol. Chem. 289 (18) (2014) 12189–12194, https://doi.org/10.1074/jbc.R114.557314.

[51] C. Arden, L.J. Hampson, G.C. Huang, J.A.M. Shaw, A. Aldibbiat, G. Holliman, D. Manas, S. Khan, A.J. Lange, L. Agius, A role for PFK-2/FBPase-2, as distinct from

[52] fructose 2,6-bisphosphate, in regulation of insulin secretion in pancreatic β-cells, Biochem. J 411 (1) (2008) 41–51, https://doi.org/10.1042/BJ20070962.

[52] S. Leng, X. Zhang, S. Wang, J. Qin, Q. Liu, A. Liu, Z. Sheng, Q. Feng, X. Hu, J. Peng, Ion Channel Piezo1 activation promotes aerobic glycolysis in macrophages, Front. Immunol. 13 (September) (2022) 1–15, https://doi.org/10.3389/fimmu.2022.976482.

[53] C. Montemurro, H. Nomoto, L. Pei, V.S. Parekh, K.E. Vongbunyong, S. Vadrevu, T. Gurlo, A.E. Butler, R. Subramaniam, E. Ritou, O.S. Shirihai, L.S. Satin, P. C. Butler, S. Tudzarova, IAPP toxicity activates HIF1α/PFKFB3 signaling delaying β-cell loss at the expense of β-cell function, Nat. Commun. 10 (1) (2019), https://doi.org/10.1038/s41467-019-10444-1.

[54] P. Gilon, H.Y. Chae, G.A. Rutter, M.A. Ravier, Calcium signaling in pancreatic β-cells in health and in type 2 diabetes, Cell Calcium 56 (5) (2014) 340–361, https://doi.org/10.1016/j.ceca.2014.09.001.

[55] P.E. MacDonald, M.B. Wheeler, Voltage-dependent K+ channels in pancreatic beta cells: role, regulation and potential as therapeutic targets, Diabetologia 46 (8) (2003) 1046–1062, https://doi.org/10.1007/s00125-003-1159-8.

[56] Henquin, J. Pathways in Beta Cell Stimulus-Secretion Coupling as Targets for Therapeutic Insulin Secretagogues. **2004**, *53* (December).

[57] A. Wendt, L. Eliasson, Pancreatic α -cells – the unsung heroes in islet function, Semin. Cell Dev. Biol. 2020 (103) (2019) 41–50, https://doi.org/10.1016/j.semcdb.2020.01.006.

[58] D.J. Lee, M.A. Cavasin, A.J. Rocker, D.E. Soranno, X. Meng, R. Shandas, D. Park, An injectable sulfonated reversible thermal gel for therapeutic angiogenesis to protect cardiac function after a myocardial infarction 11 medical and health sciences 1102 cardiorespiratory medicine and haematology, J. Biol. Eng. 13 (1) (2019) 1–13, https://doi.org/10.1186/s13036-019-0142-y.

[59] M.R. Laughter, J.R. Bardill, D.A. Ammar, B. Pena, D.J. Calkins, D. Park, Injectable neurotrophic factor delivery system supporting retinal ganglion cell survival and regeneration following optic nerve crush, ACS Biomater Sci. Eng. 4 (9) (2018) 3374–3383, https://doi.org/10.1021/acsbiomaterials.8b00803.

[60] A.J. Rocker, D.J. Lee, R. Shandas, D. Park, Injectable polymeric delivery system for spatiotemporal and sequential release of therapeutic proteins to promote therapeutic angiogenesis and reduce inflammation, ACS Biomater Sci. Eng. 6 (2) (2020) 1217–1227, https://doi.org/10.1021/acsbiomaterials.9b01758.

[61] J.R. Bardill, S.M. Williams, M.R. Laughter, D. Park, A.I. Marwan, Evaluation of scaffolding, inflammatory response, and wound healing support of a reverse thermal gel for myelomeningocele patching, J. Appl. Polym. Sci. 138 (11) (2021), https://doi.org/10.1002/app.50013.

[62] R.V. Iozzo, Matrix proteoglycans: from molecular design to cellular function, Annu. Rev. Biochem 67 (1998) 609–652, https://doi.org/10.1146/annurev.biochem.67.1.609.

[63] G.A. Paredes-Juarez, N.M. Sahasrabudhe, R.S. Tjoelker, B.J. De Haan, M. A. Engelse, E.J.P. De Koning, M.M. Faas, P. De Vos, DAMP production by human islets under low oxygen and nutrients in the presence or absence of an immunoisolating-capsule and necrostatin-1, Sci. Rep. 5 (June) (2015) 1–12, https://doi.org/10.1038/srep14623.

[64] N.L. Farnsworth, R.K.P. Benninger, New insights into the role of connexins in pancreatic islet function and diabetes, FEBS 588 (8) (2014) 1278–1287, https://doi.org/10.1016/j.febslet.2014.02.035.New.

[65] C. Wysham, J. Shubrook, C. Wysham, Beta-cell failure in type 2 diabetes : mechanisms, markers, and clinical implications beta-cell failure in type 2 diabetes : mechanisms, markers, and clinical implications, Postgrad. Med. 132 (8) (2020) 676–686, https://doi.org/10.1080/00325481.2020.1771047.

[66] P.E. Macdonald, P. Rorsman, Oscillations, Intercellular Coupling, and Insulin Secretion in Pancreatic β, Cells. 4 (2) (2006) 167–171, https://doi.org/10.1371/journal.pbio.0040049.

[67] F.M. Ashcroft, P. Rorsman, K ATP channels and islet hormone secretion : new insights and controversies, Nat. Rev. Endocrinol. 9 (11) (2013) 660–669, https://doi.org/10.1038/nrendo.2013.166.K.

[68] N.L. Farnsworth, R.L. Walter, A. Hemmati, M.J. Westacott, R.K.P. Benninger, Low Level Pro-Inflammatory Cytokines Decrease Connexin36 Gap Junction Coupling in Mouse and Human Islets through Nitric Oxide-Mediated Protein Kinase Cδ, J. Biol. Chem. 291 (7) (2016) 3184–3196, https://doi.org/10.1074/jbc.M115.679506.

[69] J. Zmazek, M.S. Klemen, R. Marković, J. Dolenšek, M. Marhl, A. Stožer, M. Gosak, Assessing Different Temporal Scales of Calcium Dynamics in Networks of Beta Cell Populations, Front. Physiol. 12 (March) (2021) 1–16, https://doi.org/10.3389/fphys.2021.612233.

[70] A. Stožer, J. Dolenšek, M.S. Rupnik, Glucose-stimulated calcium dynamics in islets of langerhans in acute mouse pancreas tissue slices, PLoS One 8 (1) (2013), https://doi.org/10.1371/journal.pone.0054638.

[71] M. Gosak, R. Yan-Do, H. Lin, P.E. Macdonald, A. Stozer, Ca2+ Oscillations, waves, and networks in islets from human donors with and without type 2 diabetes, Diabetes 71 (12) (2022) 2584–2596, https://doi.org/10.2337/db22-0004.

[72] Gosak, M.; Kri, L.; Pohorec, V.; Rupnik, M. S.; Dolen, J. Glucose-Dependent Activation , Activity , and Deactivation of Beta Cell Networks in Acute Mouse Pancreas Tissue Slices. **2024**, No. February 2021. https://doi.org/10.1152/ajpendo.00043.2021.

[73] R.K.P. Benninger, W.S. Head, M. Zhang, L.S. Satin, D.W. Piston, Gap Junctions and Other Mechanisms of Cell – Cell Communication Regulate Basal Insulin Secretion in the Pancreatic Islet. 22 (2011) 5453–5466, https://doi.org/10.1113/jphysiol.2011.218909.

[74] R.K.P. Benninger, M. Zhang, W.S. Head, L.S. Satin, D.W. Piston, Gap Junction Coupling and Calcium Waves in the Pancreatic Islet. 95 (December) (2008) 5048–5061, https://doi.org/10.1529/biophysj.108.140863.

[75] M. Yao, A. Tijore, D. Cheng, J.V. Li, A. Hariharan, B. Martinac, G.T. Van Nhieu, C. D. Cox, M. Sheetz, Force- and cell state-dependent recruitment of piezo1 drives focal adhesion dynamics and calcium entry, Sci. Adv. 8 (45) (2022) 1–15, https://doi.org/10.1126/sciadv.abo1461.

[76] M. Li, X. Zhang, M. Wang, Y. Wang, J. Qian, X. Xing, Z. Wang, Y. You, K. Guo, J. Chen, D. Gao, Y. Zhao, L. Zhang, R. Chen, J. Cui, Z. Ren, Activation of piezo1 contributes to matrix stiffness-induced angiogenesis in hepatocellular carcinoma, Cancer Commun. 42 (11) (2022) 1162–1184, https://doi.org/10.1002/cac2.12364.

[77] P. Ausina, D. Da Silva, D. Majerowicz, P. Zancan, M. Sola-Penna, Insulin specifically regulates expression of liver and muscle phosphofructokinase isoforms, Biomed. Pharmacother. 103 (March) (2018) 228–233, https://doi.org/10.1016/j.biopha.2018.04.033.

[78] G.C. Yaney, V. Schultz, B.A. Cunningham, G.A. Dunaway, B.E. Corkey, K. Tornheim, Phosphofructokinase isozymes in pancreatic islets and clonal β-cells (INS-1), Diabetes 44 (11) (1995) 1285–1289, https://doi.org/10.2337/diab.44.11.1285.

[79] M. Jiang, Y.X. Zhang, W.J. Bu, P. Li, J.H. Chen, M. Cao, Y.C. Dong, Z.J. Sun, D. L. Dong, Piezo1 channel activation stimulates ATP production through enhancing mitochondrial respiration and glycolysis in vascular endothelial cells, Br. J. Pharmacol. 180 (14) (2023) 1862–1877, https://doi.org/10.1111/bph.16050.